Discrete element model for viscoelastic materials with brittle fracture: Applications on glacier dynamics

Timo Riikilä

Academic Dissertation
for the Degree of
Doctor of Philosophy

To be presented, by permission of the
Faculty of Mathematics and Natural Sciences
of the University of Jyväskylä,
for public examination in Auditorium FYS-1 of the
University of Jyväskylä on January 27th, 2017
at 12 o'clock noon

ABSTRACT

Global warming is one of the greatest threats that mankind has to face in the beginning of this century. Affiliated with it is the incontrovertible mass loss of glacier ice in the polar regions worldwide. As a consequence, understanding the behaviour of large ice masses is crucial for estimating and, in best cases, hindering the propagation of mass loss. Traditionally, continuum models have been used to numerically study glacier dynamics. They are based on the assumption of continuous material with no substructure, therefore cracks and fragmentation are difficult to model. However, fracturing and fragmentation are inherent properties of a material as brittle as ice. Thus, better understanding of its behaviour requires incorporation of these brittle properties into the simulation model.

To tackle this shortcoming in the world of numerical physics, a new discrete element model (DEM) for studying viscoelastic materials with fracture is introduced. In DEM models, material is comprised of a large number of particles that are bound together with interaction potentials e.g. springs or beams. Fracture and fragmentation come naturally in these kinds of models through the assignment of a breaking threshold of an interaction. With the proper setting of the properties of the particles themselves and the interaction potentials between them, the material can be made to realise a wide variety of elastic, plastic and also viscoelastic behaviour.

The main focus of this study is to establish a new way to simulate viscoelastic materials with fracture. Therefore much of the work is concentrated in the validation of the model against known principles of viscoelastic and brittle materials. The model has also been used to study glacier calving and other glacier-ice related applications. Amongst other things, it was demonstrated that the behaviour of a surging glacier is strongly affected by the basal friction, that the fragment size distribution of a calving event can be a combination of fragmentation and grinding and that termini of calving glaciers can be considered as self-organized critical systems.

Keywords: discrete element method, glacier dynamics, fragmentation, fracture, viscoelastic

Author   Timo Riikilä
                    Department of Physics
                    University of Jyväskylä
                    Jyväskylä, Finland

Supervisor   Dr. Jan Åström
                    CSC - It-centre for science
                    Esbo, Finland

Supervisor   Prof. Jussi Timonen
                    Department of Physics
                    University of Jyväskylä
                    Jyväskylä, Finland

Reviewers   Dr. Jari Hyväluoma
                    Natural Resources Institute
                    Jokioinen, Finland

Reviewers   Dr. Sue Cook
                    Antarctic climate & ecosystems cooperative research
                    centre
                    Hobart, Tasmania

Opponent   Prof. Ferenc Kun
                    Department of Theoretical Physics
                    University of Debrecen
                    Debrecen, Hungary

ACKNOWLEDGEMENTS

LIST OF PUBLICATIONS

I   J.A. Åström, T.I. Riikilä, T. Tallinen, T. Zwinger, D. Benn, J.C. Moore and J. Timonen. A particle based simulation model for glacier dynamics. *The Cryosphere, 7:1591-1602*, 2013.

II   T.I. Riikilä, T. Tallinen, J.A. Åström and J. Timonen. A discrete-element model for viscoelastic deformation and fracture of glacial ice. *Computer Physics Communications, 195:14-22*, 2015.

III   J.A. Åström, D. Vallot, M. Schäfer, E.Z. Welty, S. O'Neel, T.C. Bartholomaus, Yan Liu, T.I. Riikilä, T. Zwinger, J. Timonen and J.C. Moore. Termini of calving glaciers as self-organized critical systems. *Nature Geoscience, 7:874-878*, 2014.

IV   Riikilä et al.. Brittle shear zones - the large strain limit. *Pre-print*, 2016.

Author's contribution

Publication **I** presents a new simulation model based on discrete element method to study glacier dynamics. The author has contributed to the model development and acquisition of the simulation data. Author has also contributed to the formulation of the original manuscript and has been involved in the editing process of the final published version. Publication **II** focuses on the model description, validates the model results and presents some applications of interest. The author has been mainly responsible for the original manuscript and editing process. All the results acquired in this text has been produced by the author. Publication **III** shows through simulations and experimental findings that termini of calving glaciers can be considered as self-organized critical systems. In this publication the author has been involved in the simulation model development. Publication **IV** is left out from the thesis due to slightly different application area but is strongly related to other papers. There the same simulation model was used to study the effective friction between two fracturing surfaces.

CONTENTS

ABSTRACT

ACKNOWLEDGEMENTS

LIST OF PUBLICATIONS

8

PUBLICATIONS

1 INTRODUCTION

The recurring glacial and interglacial periods have altered the living conditions and evolution for plants and animals through the history of our planet. Thus the solid state of our precious water has been a subject of human interest since the dawn of our species. Whether discussing annual variations or long-term trends of ice accumulation worldwide, the subject influences life on earth profoundly. Consequently, it is not a surprise that ice has intrigued already the more primitive societies and has been studied in a more organized fashion since the scientific revolution. Even so, still in the recent years new discoveries concerning the crystalline phases of ice has been made (Salzmann et al. 2006) and the study of mechanical properties of ice and glaciers are active fields of research.

During the last decades, the on-going increase of global average temperature has raised growing concern. A clear indicator of its effects is the negative mass balance i.e. mass loss of glacier ice worldwide. The World Glacier Monitoring Service reported in 2013, based on more than 100 glaciers worldwide, that there are ever decreasing number of glaciers with positive mass balance and that there has been no net annual positive mass balance of all the reference glaciers combined in almost three decades (Zemp et al. 2013). The mass is lost through many different processes such as melting, sublimation, evaporation and ice calving. A significant portion of the mass loss in marine terminating ice fronts results from calving (Burgess et al. 2005; Walter et al. 2010; Depoorter et al. 2013). Calving also further accelerates global warming through reduction of sunlight reflecting surface. Therefore, now more than ever, the understanding of glacier ice behavior is of utmost importance.

In the past, glaciers have been widely studied using analytical methods (Bahr 1996) and continuum based numerical models (Gilbert et al. 2014; Jarosch 2008; Le Meur et al. 2004). For example, analytically derived shallow ice equation has been used to predict the flow behaviour of an ice slab on inclined bedrock (Lüthi 2013). The equation is based on well established physical laws such as conservation of mass, force balance and Glen's flow law. Similarly, continuum based numerical models like finite element method (FEM) can be used to study the same behavior but are not restricted to simple geometries as the analytical methods of-

ten are. As long as ice can be considered as continuous material, the continuum based numerical methods are useful in predicting its behaviour. These conditions are met within the elastic and viscous limits of ice. Ice is however a very brittle material and even relatively small strain rates will induce fracturing and fragmentation. Continuum models can be accommodated for this for example by modifying the constitutive equations used for describing the material. In this way, the effects of fracturing can be simulated by reduced viscosity and stiffness. Even though this approach is useful amongst the continuous models, it can not realistically simulate the true discontinuity of fragmenting ice mass.

The main objective of this work was to build a numerical model capable of reproducing the elastic, viscous and also brittle behaviour of glacier ice. To this end, discrete element modelling (DEM) was adopted instead of continuum modelling. The basis of the DEM concept was laid by Cundall in the 1970s (Cundall 1971, 1974, 1978; Cundall and Strack 1979) but few models exist that describe all the aforementioned components necessary to simulate glacier ice. To the author's best knowledge, no such implementations in the field of glaciology have been constructed. The idea of discrete element modelling is to construct the simulated material from a large number of individual grains or particles that interact through collisions and cohesive interparticle potentials. The interparticle potentials can be given a maximum threshold of stress, strain or energy which allows the material to fracture and fragment in a natural way. Moreover, if the potentials are described in a suitable fashion, the material can be made to realise also elastic and viscous behaviour.

This thesis is structured as follows: A brief introduction to discrete element methods is given in Chapter 2. In the beginning of Chapter 3 the basic properties of glacier ice are introduced as the basis for glacier ice model construction. The rest of the chapter is used to present the glacier ice model. In Chapter 4 the simulation model is applied to selected glacier specific applications and their results are presented. In Chapter 5 the ending remarks and a brief outlook is given.

2   DISCRETE ELEMENT METHOD

The discrete element method, also called the distinct element method, is a numerical method used to simulate granular materials. The model description starts with a collection of discrete particles of varying shape and size and the forces between them. During a simulation the Newtonian dynamics of each individual particle is calculated forward by using a time integration scheme.
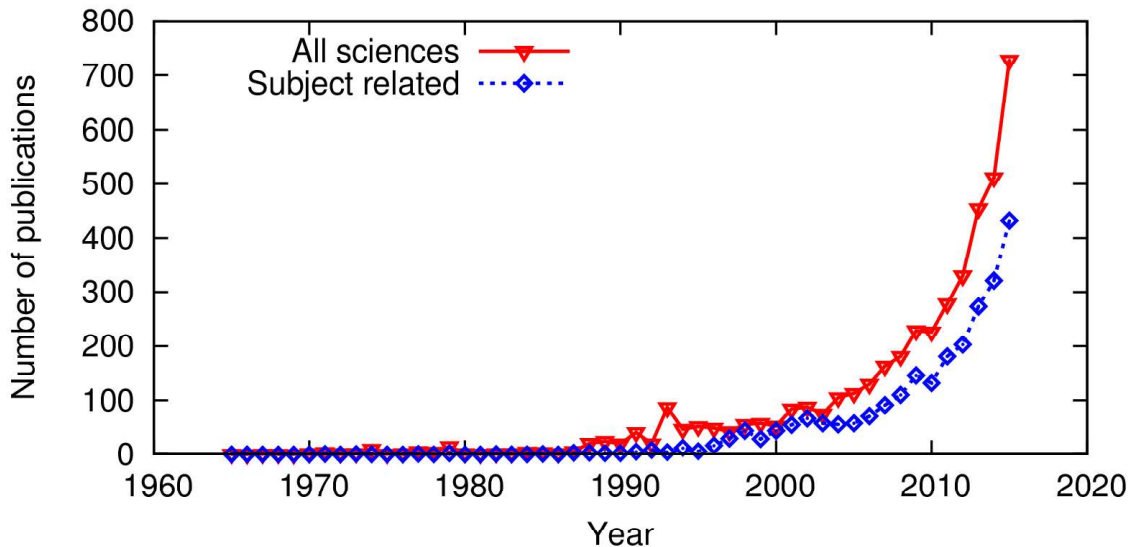
FIGURE 1   Number of publications on discrete element method versus year of publication. The statistics for each year were obtained with ScienceDirect search for the phrase "discrete element method". The two curves represent search results within all sciences and subjects related to this thesis (physics, earth sciences and material sciences).

The use of DEMs became possible in scientific research in the early 1970s with the microcomputer revolution. At the same time, Cundall published his paper where he introduced the method (Cundall 1971). In the years that followed, Cundall refined his method (Cundall 1974, 1978) and at the end of 1970s the method was val-

idated against experimental findings in his renowned paper (Cundall and Strack 1979). The number of published papers started to increase steadily as better algorithms and methods were developed and the method became more widespread (Fig. 1).
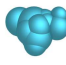
Nowadays, DEM models are used across disciplines in a great number of different applications ranging from earth and planetary sciences (Johnson et al. 2015; Kazerani 2013; Bidgoli et al. 2013) through chemical engineering (Freireich et al. 2015; Thornton et al. 2015; Wolff et al. 2013) to fragmentation of brittle and plastic materials (Carmona et al. 2014; Timár et al. 2012; Åström 2006; Kun and Herrmann 1999). In addition to the Cundall type DEM model, many different kinds of models belonging to the DEM family have been developed, namely the generalized discrete element method (Williams et al. 1985), the discontinuous deformation analysis (DDA) (Shi 1992) and the combined finite-discrete element method (FDEM) (Munjiza 2004). In this thesis the investigation is restricted only to the Cundall type of model. Even with this restriction a large variety of choices can be made about the model description. Nevertheless, there are some common features in the models that can be recognized. In this chapter these basic features are presented. Before going into the details of properties of DEM models, it is emphasized that the presentation here is not comprehensive and for further details the reader is encouraged to explore the references given in the following sections.
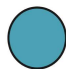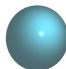
2.1 Particles

A single particle is the most basic constituent of any DEM model. The particles can be made virtually any shape or size. The most usual choice is to use spheres in three dimensions (Pál et al. 2014; Kun et al. 2014, 2013; Timár et al. 2010; Carmona et al. 2008) and disks in two (Sator and Hietala 2010; Sator et al. 2008; Åström and Herrmann 1998). Besides spheres and disks, particle shapes such as triangles (Zhang et al. 2013; Kazerani et al. 2010), higher order polygons (Nouguier-Lehon et al. 2003; Kun and Herrmann 1996), pills, cubes (Munjiza 2004) and clumped particles (Gao et al. 2012; Rong et al. 2013) are used. In general, more complex particles can be regarded to produce more realistic simulations but with a higher computational cost. The most usual particle shapes used in DEM models are shown in Table 1.

The reason for the lower computational cost of more simple particles lies in the simple collision detection and force calculation algorithms. For example, spheres can be guaranteed not to overlap if their relative distance is greater than the sum of their radii, regardless of their orientation. The same kind of simple rule cannot be formed for more complex particle shapes like cubes or tetrahedrons. Also, forces between spherical bodies usually work parallel or perpendicular to the line joining the sphere centres. This simplifies calculations and boosts efficiency. Two particle shapes from Table 1 should be pointed out. The general polygon cannot be given a single estimate of computational cost because it de-

TABLE 1   Most common particle shapes in DEM models.

Dimension	Shape		Computational cost	Example reference
2D	Disk		Low	Sator et al. (2008)
2D	Triangle		Moderate	Zhang et al. (2013)
2D	General Polygon		Moderate - High	Kun and Herrmann (1996)
3D	Sphere		Low	Kun et al. (2013)
3D	Tetrahedron		Moderate	Smeets et al. (2015)
3D	Cube		Moderate	Smeets et al. (2015)
3D	Clumped particle		Low - High	Gao et al. (2012)

pends on the number of vertices. The higher the number, the slower the computation. The same applies to the case of a clumped particle that reduces to a sphere if the subparticle number reduces to unity. Contrary to polygons, for clumped particles the computational cost does not emerge from slower collision detection algorithms because single sphere algorithms can be used. The increase in computational cost emerges in this case as a result of higher number of particles. After the choice of particles, the minimum requirement for any sensible particle system is the inclusion of contact interaction to the model. These interaction forces are the subject of the next section.

2.2   Contact interactions

In the course of a DEM simulation particles may, and usually will, come close enough to each other to make a mechanical contact. For simulations to be physically realistic and useful, the particles cannot go through each other without interaction. In this section simple interaction force schemes for spherical bodies are presented. Consider the case of two three-dimensional spheres that are in a mechanical contact and restricted to three degrees of freedom, of which one is rotational and two are translational (see Fig. 2). Fully three-dimensional treatment

has more degrees of freedom but the treatment is similar and not presented here for the sake of clarity.
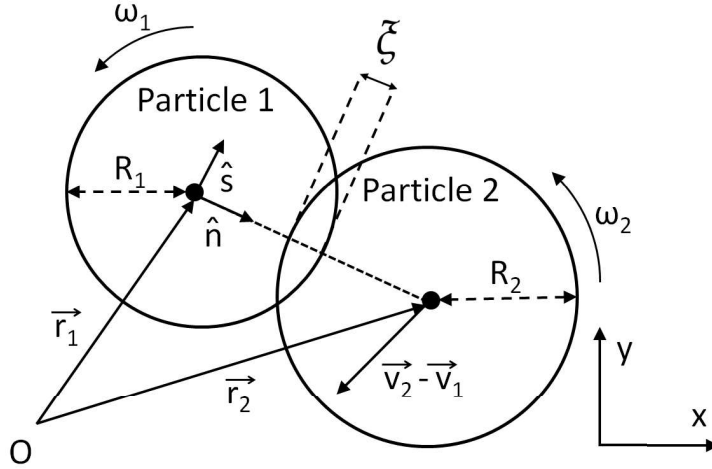
FIGURE 2 Two three-dimensional spheres in contact restricted to two-dimensional plane. In typical simulations the overlap ξ is very small compared to the particle size, in this image it has been exaggerated for clarity.

As was mentioned earlier, there is a simple rule to determine if spheres (or disks in two dimensions) are in contact which can be expressed as

$$\xi_{12} \equiv R_1 + R_2 - |\vec{r_1} - \vec{r_2}| > 0, \tag{1}$$

where the symbols refer to ones given in Fig. 2. Equation (1) does not only give a condition for mechanical contact but also a quantitative measure which can be used to calculate the forces between the particles, namely the overlap ξ (see section 2.2.1). The total force applied to one of the particles of any shape and dimension in a particle pair can be described by

$$\vec{F}_{12} = \begin{cases} \vec{F}_{12}^n + \vec{F}_{12}^s, & \text{if } \xi_{12} > 0 \\ 0, & \text{otherwise.} \end{cases} \tag{2}$$

Of course the other particle feels a force of the same magnitude but opposite direction. For the spheres in Fig. 2 the normal and tangential components in Eq. (2) can be written in the form

$$\vec{F}_{12}^n = F_{12}^n \, \hat{n}_{12} \qquad\qquad \vec{F}_{12}^s = F_{12}^s \, \hat{s}_{12}, \tag{3}$$

with unit vectors

$$\hat{n}_{12} = \frac{\vec{r_2} - \vec{r_1}}{|\vec{r_2} - \vec{r_1}|}, \qquad\qquad \hat{s}_{12} = (-\hat{n}_{12}^y, \hat{n}_{12}^x). \tag{4}$$

In the following, we always refer to the two-sphere system described in Fig. 2 and the subscript 12 is omitted. In the next subsections some ways to model the normal and tangential forces for two-sphere geometry are presented.

2.2.1 Normal forces

One of the simplest ways used to model normal force between two spheres in contact is the linear spring-dashpot model (Pöschel and Schwager 2005) given by equation

$$F^n = C_e \xi + C_d \dot{\xi}, \tag{5}$$

where C_e and C_d are the elastic and dissipative constants, respectively. Without the dissipative term the colliding particle system would not be able to lose kinetic energy and would keep moving endlessly. The time derivative of the overlap is the difference in normal velocities between the spheres i.e. the relative normal velocity

$$\dot{\xi} = \vec{v_2}^n - \vec{v_1}^n = (\vec{v_2} - \vec{v_1}) \cdot \hat{n}, \tag{6}$$

where once again the symbols refer to Fig. 2. The simplest model is not usually the most accurate one. This becomes obvious when the restitution coefficient derived from the basis of this model is examined. The restitution coefficient is defined as the ratio of postcollisional and precollisional normal relative velocities v and v', respectively. For the case of Eq. (5) it is presented in the form (Shäfer et al. 1996)

$$\epsilon \equiv \frac{v'}{v} = \exp\left[\frac{\pi C_d}{2m_{\text{eff}}} \left(\frac{C_e}{m_{\text{eff}}} - \left(\frac{C_d}{2m_{\text{eff}}} \right)^2 \right)^{-1/2} \right], \tag{7}$$

where $m_{\text{eff}} \equiv m_1 m_2 / (m_1 + m_2)$ is the effective mass of the colliding particles 1 and 2. From Eq. (7) it can be seen that ϵ is independent of the impact velocity. This, however, is not supported by experimental results according to which ϵ decreases with collision velocity (Müller et al. 2013; Shäfer et al. 1996). For a more realistic normal force, the results of the Hertz theory of elastic contact (Johnson 1985) can be used for spheres to yield

$$F^n = \frac{2Y\sqrt{R_{\text{eff}}}}{3(1 - \nu^2)} \xi^{3/2}, \tag{8}$$

where $R_{\text{eff}} = R_1 R_2 / (R_1 + R_2)$ is the effective radius of the spheres in contact, Y is the Young's modulus of the material and ν its Poisson's ratio. For dissipative behaviour, Eq. (8) must be coupled with a term which is a function of the time derivative of the overlap ξ. By choosing

$$F^n = \frac{2Y\sqrt{R_{\text{eff}}}}{3(1 - \nu^2)} \xi^{3/2} - C_d \dot{\xi}, \tag{9}$$

we get a restitution coefficient that increases with collision velocity which still contradicts experimental evidence (Shäfer et al. 1996). A better match with experiments is achieved with the form

$$F^n = \frac{2Y\sqrt{R_{\text{eff}}}}{3(1-\nu^2)}\xi^{3/2} - \widetilde{C}_d\xi^{1/2}\dot{\xi}, \tag{10}$$

where $\widetilde{C}_d$ is a function of sphere radii and two coefficients of bulk viscosity (Brilliantov et al. 1996). The properties of the force schemes presented here are not studied systematically, but a few points are worth mentioning. As in computational physics in general, a compromise between precision and efficiency has to be made. In the case of normal forces, it means that the seemingly obvious solution of choosing Eq. (10) with the most realistic behaviour for ϵ is not necessarily the most useful option. It is possible that the importance of efficiency outweighs the difference in precision. Thus, the goals of the research dictate which force models should be preferred. Secondly, the difference between a linear and non-linear dependence on the overlap ξ (e.g. Eqs. (5) and (10)) diminishes with very small values of ξ. In a simulation setup where the forces driving the spheres together are small compared to the elastic stiffness, the overlaps will remain small and the choice of normal force scheme is irrelevant. In these circumstances it pays to choose the more efficient approach. Thirdly, as Pöschel and Schwager (2005) points out, the force laws presented here may lead to an artifact of attractive normal force at some point of the collision. This results from the fact that the damping term in a force law may grow larger than the elastic part giving a negative net force. This does not happen in real particles as they do not overlap, but deform. In the receding part of the collision, the particles move away from each other faster than the deformation recovers and the particles actually detach before the damping term would grow large enough for the total force to be negative. This can be compensated in the simulations by assigning minimum normal force as zero.

2.2.2 Tangential forces

It can be justified to use only the normal forces presented in section 2.2.1. For example, if it is expected that the studied system has only a small number of particle clusters with less than two particles (see Section 2.4) the system possesses intrinsic friction due to the surface roughness of many-particle agglomerates. The same is true for simulation models where unbreakable clustered particles are used. However, it is usually preferable to include tangential forces in particle contacts to simulate friction. A simple form for tangential force often used in DEM models is

$$F^s = -\mu\,|F^n|\,\text{sign}(v^s), \tag{11}$$

where μ is the coefficient of friction and v^s the tangential component of the relative velocity between sphere surfaces i.e.

$$v^s = v_2^s - v_1^s + R_1\omega_1 + R_2\omega_2 = (\vec{v}_2 - \vec{v}_1)\cdot\hat{s} + R_1\omega_1 + R_2\omega_2. \tag{12}$$

For the symbols, see Fig. 2. The tangential force scheme given by Eq. (11) is sufficient in dynamic simulation setups but does not take into consideration the case

of static friction. When trying to simulate static arrangements of non-attached particles (like sand heaps) with Eq. (11), stable configurations can not exist. Equation (11) allows the particles to slide past each other and the system slowly diffuses. To remedy this shortcoming, different schemes that incorporate static friction has been developed. Probably the most well-known of these schemes is the one proposed by Cundall and Strack (1979) and later used by many others (Lee 1994; Tsuji et al. 1992; Zhang and Campbell 1992), namely

$$F^s = -\min(|k_\delta \varsigma| , |\mu F^n|) \cdot \text{sign}(\varsigma), \tag{13}$$

where k_δ is the tangential stiffness and ς is the tangential displacement accumulated from the time t_0 when the particles first came into contact, described mathematically as

$$\varsigma(t) = \int_{t_0}^{t} v^s(t')dt'. \tag{14}$$

The scheme given by Eq. (13) is able to reproduce static and dynamic friction. Thus, this or similar schemes should be used if static friction is relevant in the application. As in the case of normal force schemes, a more realistic presentation of the force comes with added complexity and higher costs of computation. In the case of Eq. (13) one has to add data structures for handling the tangential displacements and additional computation is needed to decide in each time step the precedence of the two possible values for the tangential force.

The force schemes for more complicated particles are not presented in this thesis but more information can be found from e.g. Pöschel and Schwager (2005), where in particular a rigorous treatment of contact forces for triangular particles is presented. In this and the previous section the simple contact force schemes for spherical particles were presented and Eq. (1) was used as a rule to determine whether the particles are in contact. To calculate the overlap of each particle pair in a simulation of thousands or even millions of particles is, however, very time-consuming and soon becomes the bottle-neck of the program. The next section focuses on this problem.

2.3 Nearest neighbour detection algorithms

2.3.1 Brute force nearest neighbour algorithm

A straightforward way to calculate the effects of particle-particle interactions would involve computing the contact forces for all particle pairs in the system (Verma et al. 2014). Such an approach may be useful for small number of particles as the implementation is by far easier than any of the competing methods and the absolute computational time may not be excessively long. For larger systems, this method becomes impractical. To illustrate the point, let us consider the case

of N disks of equal radius. Each disk in this system has $N - 1$ other disks which it can collide with. Because each interaction between two disks is calculated only once there are $N(N-1)/2$ force calculations. In a two-dimensional system of equal sized disks, each particle has a maximum of 6 direct neighbours. Then the total amount of necessary calculations is roughly $6N/2$ if the boundary effects of the lattice are omitted. Now the efficiency of brute force nearest neighbour algorithm (BFNNA) as a function of disk number can be defined as the ratio of actual calculations and the necessary calculations as

$$E_{BF} = \frac{6N/2}{N(N-1)/2} = \frac{6N}{N(N-1)} = \frac{6}{N-1}. \tag{15}$$

The graph of the efficiency of the BFNNA together with other algorithms that we will discuss in the following subsections are shown in Fig. 3. As can be seen from the image, the efficiency of the BFNNA drops quickly after 10 disks and at 1000 disks it is already pretty useless. Modern computers can still run easily with 1000 disks but a lot of time is wasted on unnecessary calculations. Of course, for every non-contacting disk only a single if-statement is evaluated compared to the full contact force calculations of contacting ones. This increases the efficiency by a constant factor but does not change the overall behaviour.
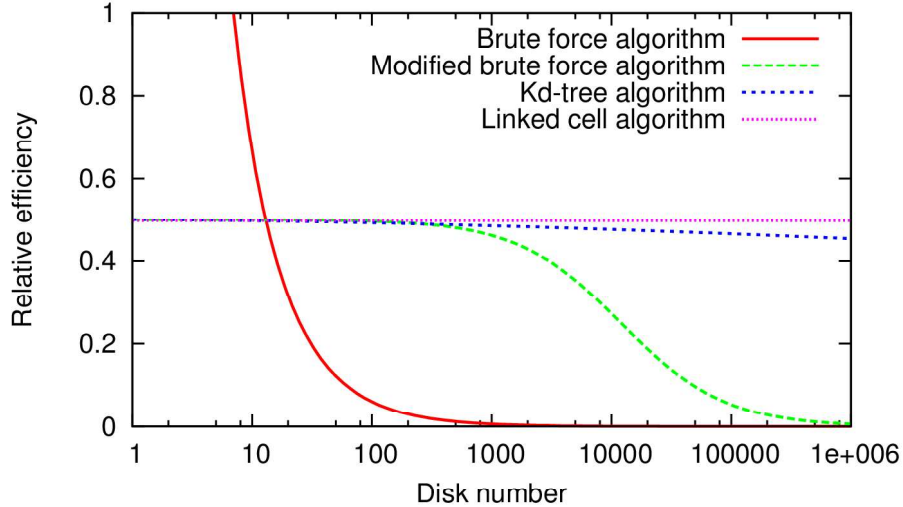
FIGURE 3   Efficiencies of different nearest neighbour algorithms as a function of disk number. Efficiency is evaluated as the ratio of actual calculations and necessary calculations.

2.3.2 Modified brute force nearest neighbour algorithm

To keep this simple approach to nearest neighbour search but to increase its efficiency, the modified brute force nearest neighbour algorithm (MBFNNA) can be used. In this approach, the neighbour search is done only occasionally and the nearby disks of each disk are saved in a data structure. This approach relies on

the valid assumption that disks that are close to each other at one moment will remain close to each other for a number of future time steps (the subject of time integration and time steps will be addressed in section 2.5). In a typical procedure the distances between all the disk pairs are calculated and for each disk a list of disks closer than a predescribed threshold distance d_{th} are saved. The evaluation of a suitable number of time steps between updates can be made in many ways. One possible way is to find the maximum speed $v_{\max}$ amongst all the disks in the system at a certain time step and then calculate the time steps necessary for two disks at the edge of d_{th} moving at maximum velocity to reach each other. For example, if the maximum velocity in the lattice at time step 0 is found to be $v_{\max} = 10 \ m/s$, the threshold distance is assigned as $d_{th} = 3 \ m$, the radii of all the disks are $r_i = 0.5 \ m$ and the time step length is $\Delta t = 0.0001 \ s$, we can evaluate the number of time steps between updates to be

$$ n = \frac{d_{th} - 2r_i}{2V_{\max}\Delta t} = \frac{3 \ m - 2 \cdot 0.5 \ m}{2 \cdot 10 \ m/s \cdot 0.0001 \ s} = 1000. \tag{16} $$

Notice that in the numerator of Eq. (16) the disk radii are subtracted from the threshold distance. This is done because the distance is usually evaluated between the centres of the disks but the contact starts when the edges collide. This approach is not infallible, however. The disk velocities are evaluated in the beginning of an update-free period and of course they can accelerate. One has to be aware of this possibility and an application specific safety factor can be used. For example, a factor of 2 could be used in Eq. (16) and an update interval of 500 time steps would be achieved, still a lot faster than the pure BFNNA.

Another safe method for assigning the update interval is to keep track of each disk during the simulation. When any of the disks has moved a distance of $(d_{th} - r_i)/2$ the update is initiated. This approach is safe since in the worst case scenario another disk has moved exactly the same distance towards the first disk and the two are just starting to collide provided that they were exactly the distance d_{th} apart in the beginning of the update free period. The probability for this to happen in a simulation of thousands of disks is diminishingly small. Therefore a weaker condition can be used, for example by doubling the distance required for any of the disks to move before update. This of course destroys the unerringness of the approach but increases its efficiency. No general guidelines can be given about the preference of maximum velocity or disk tracking approach since the overall computational cost depends a lot on the actual implementation and application.

The efficiency of the maximum velocity approach can be estimated as follows: The update step takes as long as one step in the BFNNA but its cost can be divided equally to steps with no updates. Also, at every time step, the neighbour list for all N disks is processed. Let us use an update interval of 1000 time steps. The total efficiency for the MBFNNA is then given by

$$ E_{MBF} = \frac{\frac{6N}{2}}{\frac{N(N-1)}{2} \cdot \frac{1}{1000} + \frac{6AN}{2}} = \frac{6000}{N - 1 + 6000A}, \tag{17} $$

where A is a factor related to the calculation of forces for one disk using the neighbour list. If the value of d_{th} is small enough only the nearest neighbours are calculated and $A = 1$. However, this leads to a smaller number of update free time steps. In Fig. 3 a value of $A = 2$ has been used. It is evident that the modification of the BFNNA is highly profitable. Nevertheless, as the disk number increases the time taken by the update step starts to dominate and eventually the efficiency drops close to zero. The efficiency drop results from the $O(N^2)$ complexity of the nearest neighbour detection algorithm. To reach larger values of particle number, an algorithm with lower complexity must be used. In the following sections two more efficient methods are introduced.

2.3.3 K-dimensional tree algorithm

The k-dimensional-tree (k-d tree) algorithm is based on division of space into smaller regions so that nearest neighbours are searched for only in the immediate surroundings of the particle in question (Verma et al. 2014). Here the algorithm is presented for a system of disks of equal size. Generalisation to a case of three-dimensional spheres of random size is straightforward. The process has two stages. First, the disks are arranged in a binary tree structure according to their locations. Second, the tree is used to find neighbours for each disk by navigating in space using the constructed tree as a map. To build the tree, consecutive divisions of space in x- and y-directions are performed. In Fig. 4 the first three steps of such a process in a 9 disk system are presented.
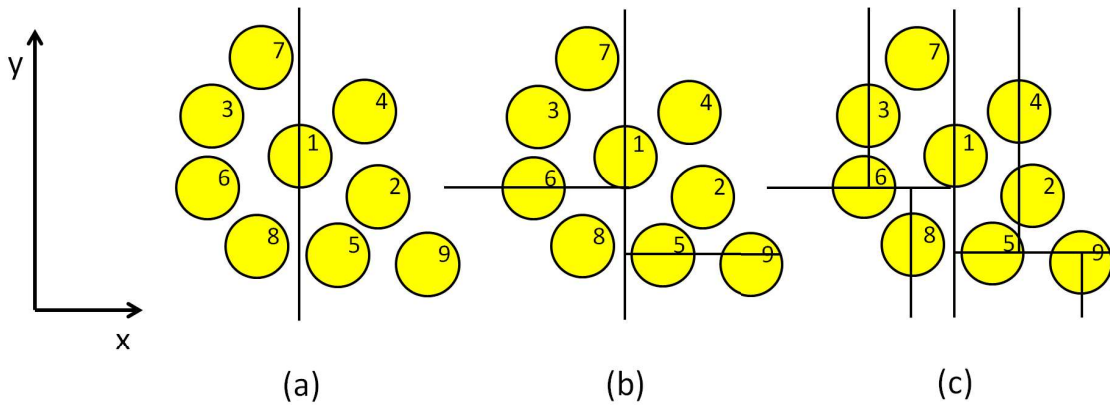
FIGURE 4   Division of disks in regions according to k-d tree algorithm. In (a) the middle disk in the x-direction is used as the centre point of division. In (b) and (c) the same is done for the subregions in y- and x-directions, respectively.

The first spatial division is done either in x- or y-direction. In Fig. 4 x-direction is used. The disk acting as a divider is chosen by sorting the disks according to their x/y-coordinates and choosing the one in the middle. If there is an even number of disks, then the first of the middle pair is chosen. This division with alternating horizontal and vertical lines continues until there are no disks left in the subdomains. The first divider disk becomes the root node of the k-d tree

and every following divider becomes a parent in its own layer. To illustrate the buildup of a k-d tree, the tree is shown in Fig. 5 for each of the three steps of Fig. 4.

Layer 1: X-division

Layer 2: Y-division

Layer 3: X-division

(a) (b) (c)
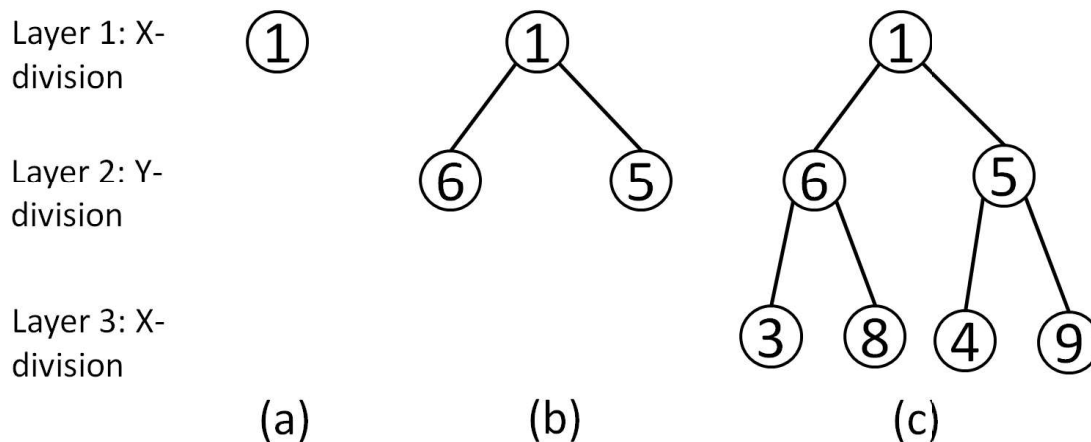
FIGURE 5   Phases (a), (b) and (c) corresponding to the three phases shown in Fig. 4

The k-d tree is constructed in a way that the nearest neighbours of any disk are found by processing only a very small fraction of the entire tree. For example, if we are interested in the neighbours of disk 6 in Fig. 4 and the nearest neighbour distance is set as 3 r_i, it is impossible that such neighbours could be found in the right branch of the tree. Similar assessments can be made for most of the branches and it turns out that the complexity of finding the neighbours of any single disk is on average $O(\log N)$. Next we derive the total efficiency of the k-d tree algorithm. First, we have to build the tree to be able to use it. In every layer of the tree the disks have to be arranged according to their x- or y-coordinates. In this example, we assume that merge-sort algorithm for sorting is used. The complexity of merge-sort is $O(N\log N)$. For each layer the sorting has to be done to each new subregion, so the total cost for building the tree is

$$C_{TB} = BN\log N + 2B \cdot \frac{N}{2}\log\frac{N}{2} + 4B \cdot \frac{N}{4}\log\frac{N}{4} + \cdots, \qquad (18)$$

where B is a constant representing all the operations related to the sorting. It can be assumed that the total amount of these operations is proportional to the total amount of particles to be sorted. The value for B cannot be given a single value, it depends a lot on the actual implementation. In the tail of Eq. (18) there will be deviation from the pattern due to uneven division of particles but here it is assumed that the particles are evenly divided. This assumption simplifies the calculations and has no effect on the overall efficiency. Equation (18) can be further modified to yield

$$
\begin{aligned}
C_{TB} &= B \cdot N \left(\log N + \log \frac{N}{2} + \log \frac{N}{4} + \cdots \right) \\
&= B \cdot N \left(\log \left[N \cdot \frac{N}{2} \cdot \frac{N}{4} \cdots \right] \right).
\end{aligned}
\tag{19}
$$

The square brackets in Eq. (19) contain $\log N$ terms and can be expressed in the form

$$
C \cdot N^{\log N},
\tag{20}
$$

where the constant C is

$$
C = 2^{-\frac{\log N (1 + \log N)}{2}}.
\tag{21}
$$

Further modifications of Eq. (19) leads to

$$
\begin{aligned}
C_{TB} &= BN(\log(C \cdot N^{\log N})) = BN(\log C + \log N^{\log N}) \\
&= BN\log C + BN\log^2 N.
\end{aligned}
\tag{22}
$$

By substituting C from Eq. (21) and modifying we finally arrive at

$$
C_{TB} = \frac{BN}{2} \left(\log^2 N - \log N \right).
\tag{23}
$$

Complexity of searching from the tree was already mentioned before and for N disks its cost is $C_{ST} = DN\log N$, where D is constant number of operations related to searching neighbours for one disk. Finally the efficiency can be calculated by using the same idea as in the MBFNNA that updates are done only once in 1000 time steps to yield

$$
\begin{aligned}
E_{KDT} &= \frac{\frac{6N}{2}}{\frac{\frac{BN}{2}\left(\log^2 N - \log N\right) + DN\log N}{1000} + A\frac{6N}{2}} \\
&= \frac{6N}{2} \cdot \frac{1000}{\frac{BN}{2}\left(\log^2 N - \log N\right) + DN\log N + 3000AN} \\
&= \frac{6000}{B\left(\log^2 N - \log N\right) + D\log N + 6000A}.
\end{aligned}
\tag{24}
$$

The parameters A, B and D affect the efficiency curve but do not change its basic shape. In Fig. 3 we have used $A = 2$ as in the case of MBFNNA, $B = 5$ and $D = 25$. As can be seen from Fig. 3 the efficiency of k-d-tree algorithm follows the MBFNNA curve up to roughly 1000 particles, but with particle systems larger than that it becomes more efficient. There is however a price to pay for better efficiency and it is added complexity. Programming kd-tree algorithm involves using several data structures and usually use of recursive algorithms which are

a lot harder to comprehend than the simple algorithms described earlier, usually based on iterative calculations. Another method, which is sort of a combination of BFNNA and k-d tree algorithms, is presented in the next section.

2.3.4 Linked cell algorithm

The basic idea behind the linked cell algorithm (LCA) is similar to k-d tree algorithm but the approach is simpler (Pöschel and Schwager 2005). Instead of building a tree to help navigating the space, the whole disk region is covered with a grid such as that exemplified in Fig. 6. Let us consider the case of finding nearest neighbours of the purple disk in Fig. 6. First, each disk is assigned in exactly one cell of the grid. It doesn't matter if some cells are left empty but the grid should be large enough to cover the whole region where the disks reside. In the next step, the distance from the purple disk to every other disk in its own and the nearest cells is calculated (green and yellow cells in Fig. 6). If the distance is less than a predescribed threshold distance, the disk in question is saved in the nearest neighbour list of the purple disk. The procedure is astonishingly simple and, as we shall see, also very efficient with large values of disk number. The complexity for assigning disks to cells is a linear process where each disk is accessed, its coordinates are read and the correct cell is determined. Thus the complexity for this process is $O(N)$. As might be expected the inspection of nearest neighbours is also a linear process of complexity $O(N)$. The constants B and C are related to the operations in assigning disks to cells and finding the disks in the nearest cells, respectively. The constant C depends on the size of the cells. The larger the cells, the more work is done checking them and correspondingly larger the factor C. Using these estimates we are ready to calculate the efficiency of the whole algorithm, and once again we will do the update only once in every 1000 time steps. The efficiency can be written as

$$
\begin{aligned}
E_{LCA} &= \frac{\frac{6N}{2}}{\frac{(B+C)N}{1000} + A\frac{6N}{2}} \\
&= \frac{6N}{2} \cdot \frac{1000}{(B+C)N + 3000AN} = \frac{3000}{B+C+3000A}.
\end{aligned}
\tag{25}
$$

Notice that the efficiency for LCA does not depend on the number of disks. Thus, for very large systems LCA appears to be the obvious choise. In Fig. 3 the efficiency of the LCA is plotted with $B = 5$, $C = 25$ and as in earlier cases $A = 2$. At this point it should be emphasized that the preferential order of nearest neighbour algorithms at certain disk number as portrayed by Fig. 3 is only approximate. The parameters for each curve are highly dependent on the actual implementation. Of course, eventually when the disk number is increased the approach that does not depend on the disk number prevails.

In conclusion, pure BFNNA is hardly ever a practical option but its modified version might be quite sufficient for small systems. With large systems, the k-d tree algorithm or LCA should be preferred. However, there are other reasons
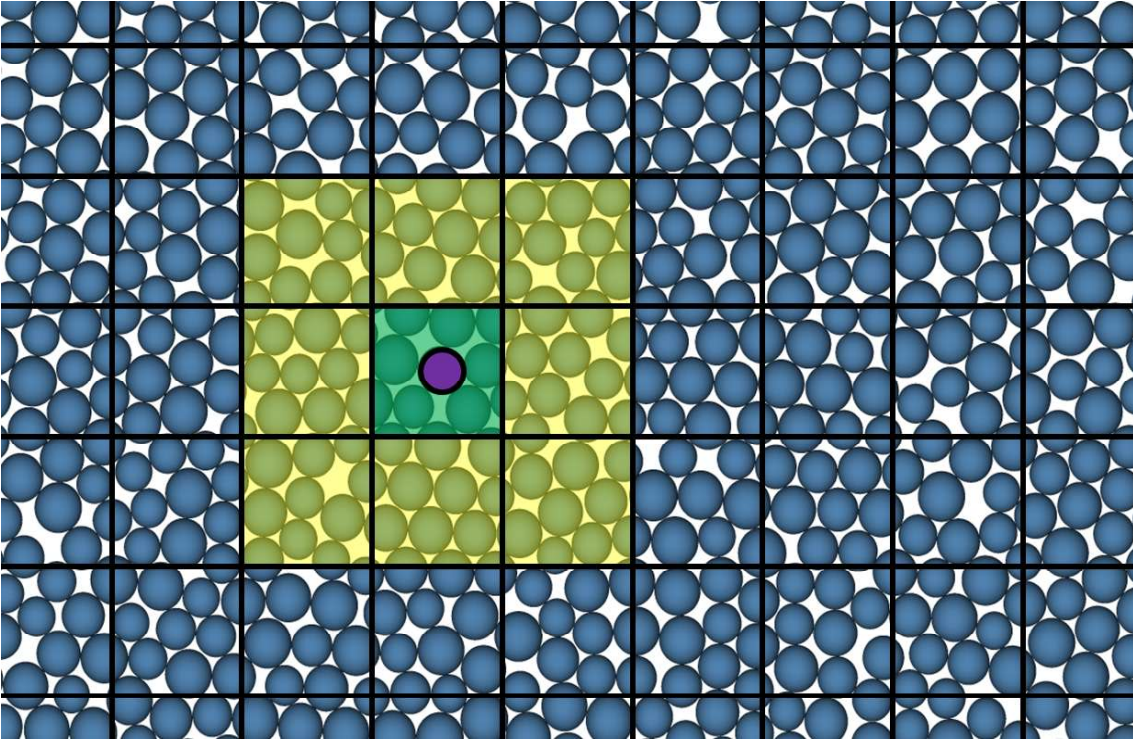
FIGURE 6   Grid used in linked cell algorithm.

that make LCA even more appealing compared to k-d tree algorithm. Firstly, it is conceptually simpler and easier to program. Secondly, because of its simplicity the parallellisation is quite straightforward.

2.4   Cohesive interactions

In addition to the forces described in section 2.2, cohesive interactions can be formulated to simulate intact solid materials. The force schemes used in this context are as numerous or even more so than in the case of contact interactions. In this section, some simple cohesive force schemes are presented and more complicated ones are discussed.

2.4.1 Linear spring model

One of the simplest ways to model a cohesive interaction between individual particles is the linear spring model illustrated in Fig. 7 (a). The model is motivated by the fact that many materials behave linearly as a function of elongation and compression when the deformation is small (Sadd 2009). This applies quite accurately to brittle materials until failure.

The mathematical description of the scheme is actually almost identical to the spring-dashpot model given by Eq. (5) in section 2.2.1. In this case however, the overlap ξ is replaced by the deformation length d of the spring and the force
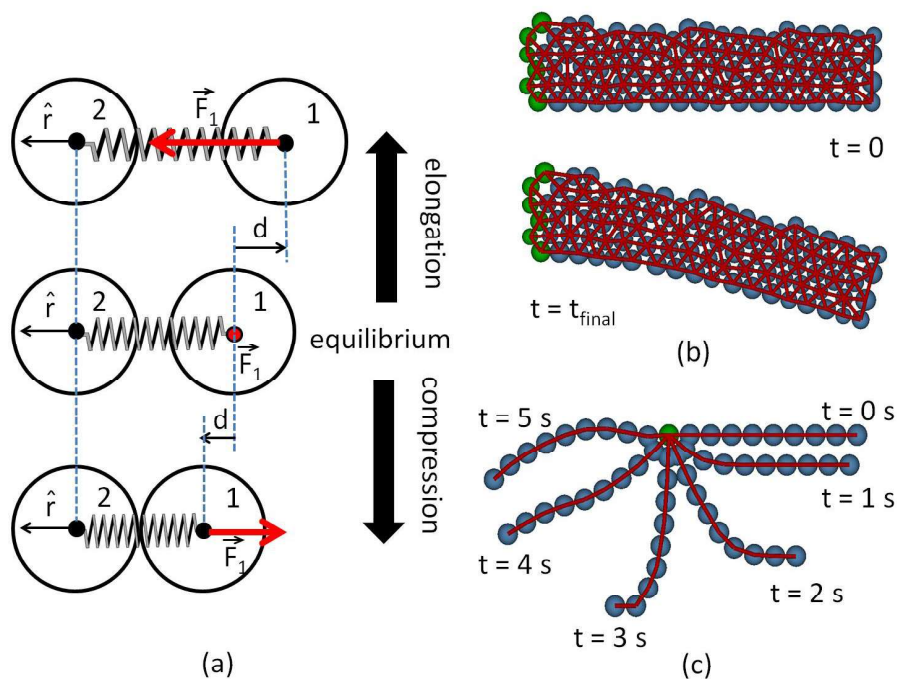
FIGURE 7 (a) Schematic presentation of forces in linear spring force scheme. Multiple row (b) and a single row (c) cantilever beam simulated with linear spring model. Green disks are rigid and the red lines represent springs.

is calculated both in compression and in elongation. If disks 1 and 2 are attached to each other with a linear spring (see Fig. 7 (a)), the forces felt by the disks are

$$
\begin{aligned}
\vec{F}_1 &= (k_s d + k_d \dot{d})\hat{r} \\
\vec{F}_2 &= -(k_s d + k_d \dot{d})\hat{r},
\end{aligned}
\tag{26}
$$

where k_s and k_d are the elastic stiffness coefficient and damping coefficient, respectively. The damping term $k_d \dot{d}$ is used to dissipate energy, otherwise the material would oscillate endlessly when disturbed. The actual choice of the elastic and damping coefficients depends on the simulated material. Coupling of the parameters to glacier ice specific properties is presented in section 3.2. The scheme is certainly appealing due to its simplicity and resulting computing efficiency. Nevertheless, the scheme has some serious drawbacks. As the forces apply only in the axis joining the disk centres, there exists no bending stiffness. This might not be a serious problem in systems where chains of disks connected with single springs rarely appear, but if they do, rather unrealistic behaviour occurs. To illustrate this behaviour, two-dimensional cantilever beams under the influence of gravity are simulated using multiple and single rows of disks (Fig. 7 (b) and Fig. 7 (c), respectively). As can be seen, the multiple row beam can withstand shear stresses and attains a stable bent configuration. The chain of disks and beams in Fig. 7 (c), on the other hand, behaves like a string with weights bound to it. There is no need to emphasize that it models the cantilever beam behaviour quite

unrealistically. There is no difference in the behaviour of single springs in the two cases. As a whole the multirow case acts more realistically however because the diagonal springs stiffen the beam so that it cannot bend freely. To attain a greater level of reality, the linear spring model must be expanded with bending stiffnesses. Usually, with this addition the springs are no longer called springs but beams.

2.4.2 Shear beam model

A simple addition to the linear spring model to attain bending stiffnesses involves retaining forces proportional to the bending angles θ_1 and θ_2 of the disks away from the beam axis. A deformation event according to this scheme is shown in Fig. 8.
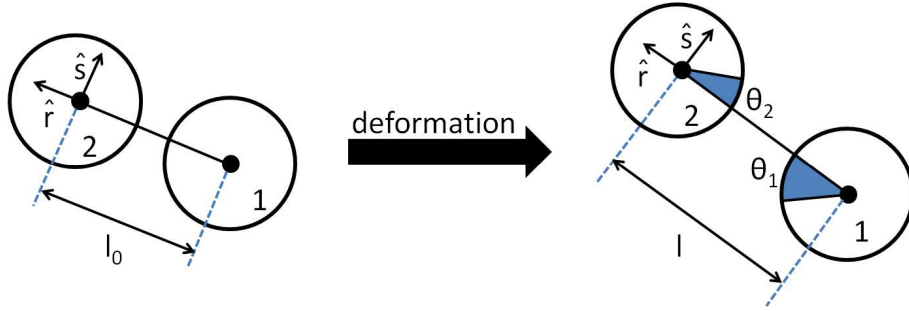
FIGURE 8   A beam between disks 1 and 2 in its equilibrium state and after deformation.

The forces for disks 1 and 2 in interaction are calculated similarly to the case of a linear spring model, but additional terms are included i.e.

$$\vec{F}_1 = (k_s d + k_{d1}\dot{d})\hat{r} - \frac{k_b(\theta_1 + \theta_2)}{l}\hat{s} = -\vec{F}_2, \tag{27}$$

where k_s and k_b are the axial and bending stiffness parameters, respectively. The damping coefficient from Eq. (26) is renamed as k_{d1} to distinguish it from the other damping coefficient needed in this approach but its meaning remains the same. The directions of the unit vectors $\hat{r}$ and $\hat{s}$ are shown in Fig. 8 and d is the difference in beam length between equilibrium and deformed state i.e. $d = l - l_0$. The description of the force scheme with Eqs. (27) is not complete because torques have to be also considered. They can be expressed in the form

$$
\begin{aligned}
\tau_1 &= k_b\theta_1 - k_{d2}\dot{\theta}_1 \\
\tau_2 &= k_b\theta_2 - k_{d2}\dot{\theta}_2,
\end{aligned}
\tag{28}
$$

where k_{d2} is the bending damping coefficient. The second term in the right hand side of Eq. (28) is used to damp the rotational degree of freedom. Although the shear beam model can induce bending stiffness and the stiffness parameters can be adjusted for a large system of beams to yield desired elastic parameters (see

section 3.2), a single beam has the same properties regardless of its cross-sectional area and length. It is obvious that these geometrical aspects affect the behaviour of a single beam and for a better level of reality the programmer might use Euler-Bernoulli or Timoshenko beams (Seon et al. 1999). Both of these models take into consideration the properties of individual beams but Timoshenko beams model shearing behaviour more realistically (Ghugal and Sharma 2011). By using continuous potentials like Lennard-Jones potential (Thomson et al. 2014) for contact interaction, no additional cohesive interaction model is needed since the contact interaction scheme models both cohesion and repulsion. Plastic and viscoelastic cohesive force models are not presented here but an example of a viscoelastic model is presented in section 3.2 for glacier ice in which the viscoelasticity is achieved by using breaking and reforming beams. Interaction breakdown in general is the subject of the next section.

2.4.3 Interaction breakdown

One of the appealing properties about DEM models is that fracturing of brittle materials is easy to implement into the simulation model. For the case of continuous potentials e.g. Lennard-Jones potential, the breakdown comes naturally as the cohesive force between the particles vanishes continuously. For harmonic potentials e.g. shear-beams introduced in Section 2.4.2, the retaining force grows linearly as a function of distance and the beam will not break unless otherwise stated. The removal of the beams from the simulation is simple and straightforward procedure but the removal cannot be made at random. There has to be a physical rule that controls the breakdown. As usual for DEM models, the choice of this rule is not unambiguous.

In the following we will focus only on tensile stress states in two dimensions. Compressive and three dimensional cases are treated similarly but not handled here. There are many fracture criteria used with DEM models. One of them is the maximum normal stress criterion (Sochor 1998)

$$\sigma_{\mathrm{max}} \geq \sigma_0, \tag{29}$$

where σ_{max} is the maximum normal stress and σ_0 is the critical normal fracture stress. This condition is realized only when the fracture surface is perpendicular to the applied normal stress (Zhang and Eckert 2005). A schematic view of a two-dimensional tensile stress scenario is shown in Fig. 9 with fracture surfaces produced with different fracture criteria. The Tresca failure criterion gives a failure condition as (Zhang and Eckert 2005)

$$\tau_{max} \geq \tau_0, \tag{30}$$

where τ_{max} and τ_0 are the maximum shear stress and the shear fracture stress. The maximum shear stress occurs on a plane inclined by 45° with respect to the tensile stress axis. Another criterion for tensile failure is the Mohr-Coulomb stress criterion, which postulates that the shear failure depends on both the shear and normal stress i.e.
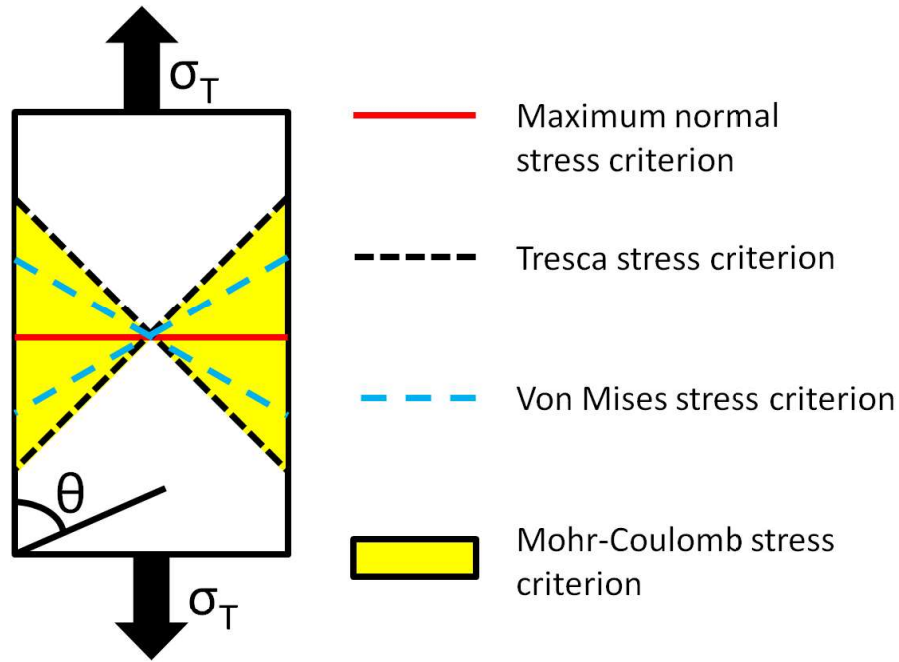
FIGURE 9   Fracture plane angles produces by different fracture stress criteria.

$$\tau + \mu \cdot \sigma \geq \tau_0, \tag{31}$$

where μ is a positive constant with range $0 < \mu < \infty$ giving a fracture plane angle $45 < \theta < 90$ thus never reaching 45 or 90 degrees exactly. Yet another stress criterion, called von Mises stress criterion, has the fracture plane at 60° from the tensile stress axis. All the stress criteria given above contain some shortages. Maximum normal, Tresca and von Mises stress criteria all depict a failure event where the fracture surface is at a given angle compared to the tensile stress axis. According to experimental evidence (Lee et al. 2004; Zhang et al. 2003; Inoue et al. 2001; Liu et al. 1998), a wide variety of fracture angles have been observed. Thus, any of the three mentioned criteria alone is not valid for general material. Mohr-Coulomb stress criterion on the other hand is more suitable for a wide variety of materials but cannot explain the limiting case of $\theta = 90^o$. Due to these limitations Zhang and Eckert (2005) propose a more general criterion called ellipse criterion which can be expressed in the form

$$\frac{\sigma^2}{\sigma_0^2} + \frac{\tau^2}{\tau_0^2} \geq 1. \tag{32}$$

According to this criterion the tensile failure of the material is controlled both by normal stress σ and the shear stress τ but not in a linear way like in Mohr-Coulomb criterion. The ratio $\alpha = \tau_0/\sigma_0$ can be used to yield a failure plane angle of $45 \leq \theta \leq 90$ thus unifying all the criteria in a single rule.

The preferred definition of stresses σ and τ depends on the particular DEM model used. For example, in the case of beams the normal and shear stresses come naturally from the beam stress state and can be used in Eq. (32). Alter-

natively to the stress based criteria described in this section, energy thresholds can be used. This approach is not presented here but an example is presented in section 3.2 during the glacier ice DEM model formulation.

2.5 Time integration

So far we have established how to calculate the forces that apply to particles in DEM simulations and how to make sure that only necessary interactions are considered. But how are these forces translated to physical movement of the particles that mimics the way particles behave in real physical world. Let us consider an example of an object in a one-dimensional free fall scenario starting from the rest. The wind resistance and all other possible forces except gravity are neglected. In this scenario it is a task of rudimentary physics to derive the equation of motion of the particle as

$$y(t) = \frac{1}{2}gt^2, \tag{33}$$

where g is the acceleration of gravity and t is the elapsed time. The direction of y-coordinate is chosen to point in the direction of gravity, so that the value of g is 9.8 m/s. To find out the y-coordinate at any moment of time t it is easily calculated with Eq. (33) as it is a continuous function of time. Computer programs are not however continuous, they are discrete. The program must be given specific instructions on how to acquire the value of particle location in the next time step based on its current position. A simple scheme to use in the free fall case could be to consider the acceleration and velocity of the particle to remain constant for the duration of the time step. This would give us update rules in the form

$$
\begin{aligned}
v_{t+\Delta t} &= v_t + g\Delta t \\
y_{t+\Delta t} &= y_t + v_t\Delta t,
\end{aligned}
\tag{34}
$$

where Δt is the length of the time step. Because acceleration is constant, this approach gives exact values for the velocities but the positions are approximations. In Fig. 10 the exact value for the y-coordinate along with four curves representing different choices for the time step Δt are shown.

As is evident, the accuracy of the approximation gets better with decreasing time step length Δt, which can be stated as a rather general rule amongst all the time integration schemes. Of course, in the case of free fall, a higher order integration scheme could have been used to yield exact solutions with all values of Δt, but this was only presented as an example. In typical DEM simulations the actual equations of motion might be highly complicated and approximate schemes must be used. In the following, a few of these schemes are presented. A more comprehensive presentation of the schemes presented here, and additional ones, is shown in Kruggel-Emden et al. (2008).
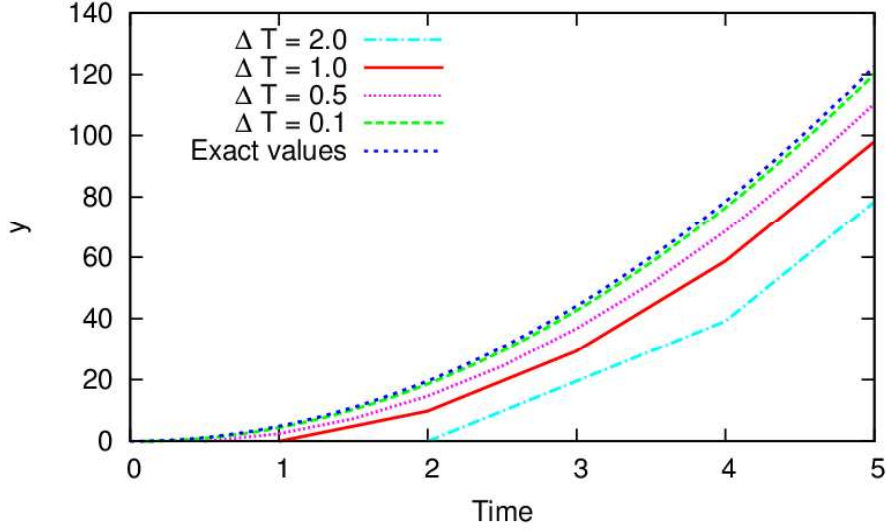
FIGURE 10   Accuracy of time integration algorithm of Eq. (34) with different time step
        sizes.

Time integration schemes can be divided into three different categories, namely
the one-step, multi-step and predictor-corrector algorithms. Actually we already
saw an example of one-step algorithm in the case of time integration of freely
falling body. The algorithm in question was the forward Euler method which can
be expressed in a general form as

$$
\begin{aligned}
\vec{r}_{t+\Delta t} &= \vec{r}_t + \vec{v}_t \Delta t \\
\vec{v}_{t+\Delta t} &= \vec{v}_t + \vec{a}_t \Delta t.
\end{aligned}
\tag{35}
$$

Here and hereafter $\vec{a}$ is the acceleration caused by all the possible forces described
in earlier sections on a particle with mass m_p i.e. $\vec{a} = \vec{F}_{tot}/m_p$. The forward Euler
method is certainly appealing due to its simplicity and it has been widely used
in a large number of papers like Di Renzo and Di Maio (2004); Melheim (2005);
Taguchi (1992a). The forward Euler scheme is actually a truncated Taylor series
restricted to the first two terms. To have a more accurate scheme, more terms can
be added to the series. For example, a scheme referred to as TY2 (Kruggel-Emden
et al. 2008) can be expressed as

$$
\begin{aligned}
\vec{r}_{t+\Delta t} &= \vec{r}_t + \vec{v}_t \Delta t + \frac{1}{2}\vec{a}_t \Delta t^2 \\
\vec{v}_{t+\Delta t} &= \vec{v}_t + \vec{a}_t \Delta t.
\end{aligned}
\tag{36}
$$

It has been applied for example in Taguchi (1992b). Arbitrarily high order ex-
pansions can of course be constructed but the computational cost increases with
every additional term. Another one-step scheme is the central difference or Verlet
algorithm which can be presented in the form

$$
\begin{aligned}
\vec{v}_{t+\Delta t/2} &= \vec{v}_{t-\Delta t/2} + \vec{a}(\vec{r}, \vec{v}_{t-\Delta t/2})\Delta t \\
\vec{r}_{t+\Delta t} &= \vec{r}_t + \vec{v}_{t+\Delta t/2}\Delta t.
\end{aligned}
\tag{37}
$$

As opposed to the integration schemes above, in Verlet algorithm velocities and positions are calculated for time steps that are $\Delta t/2$ apart. If the scheme is applied to force calculations that depend on the position and velocity, as they usually do in DEM simulations, forces need to be calculated based on velocities and positions that are $\Delta t/2$ apart. The Verlet algorithm is in use in many applications such as Cundall and Strack (1979); Kwapinska et al. (2006); O'Sullivan and Bray (2004).

In multi-step algorithms, the results from previous time steps are stored and used to calculate values of future velocities and positions. For example the fifth order Adams-Bashford scheme can be expressed in a form

$$
\begin{aligned}
\vec{r}_{t+\Delta t} &= \vec{r}_t + \Delta t(\delta_1\vec{v}_t - \delta_2\vec{v}_{t-\Delta t} + \delta_3\vec{v}_{t-2\Delta t} - \delta_4\vec{v}_{t-3\Delta t} + \delta_5\vec{v}_{t-4\Delta t}) \\
\vec{v}_{t+\Delta t} &= \vec{v}_t + \Delta t(\delta_1\vec{a}_t - \delta_2\vec{a}_{t-\Delta t} + \delta_3\vec{a}_{t-2\Delta t} - \delta_4\vec{a}_{t-3\Delta t} + \delta_5\vec{a}_{t-4\Delta t}),
\end{aligned}
\tag{38}
$$

where the constants $\delta_1 - \delta_5$ are $\delta_1 \approx 2.64$, $\delta_2 \approx 3.85$, $\delta_3 \approx 3.63$, $\delta_4 \approx 1.77$ and $\delta_5 \approx 0.35$. Different order of schemes are constructed by changing the number of terms and adjusting parameters δ_i. The Adams-Bashford time integration scheme has been used amongst many others by Takeuchi et al. (2004); Sundaram and Collins (1996).

Predictor-corrector algorithms use an initial prediction of the solution in an upcoming time step which is then altered with the corrector phase to arrive at more accurate solution. The initial prediction is based on an explicit scheme. For example, in the Gear schemes the predictor step involves calculations of Taylor series expansions. From these expansions the positions and their higher derivatives are acquired i.e.

$$
\begin{aligned}
\vec{r}_{t+\Delta t,p} &= \vec{r}_t + \vec{v}_t\Delta t + \frac{1}{2}\vec{a}_t\Delta t^2 + \frac{1}{6}\vec{b}_t\Delta t^3 + \frac{1}{24}\vec{c}_t\Delta t^4 \\
\vec{v}_{t+\Delta t,p} &= \vec{v}_t + \vec{a}_t\Delta t + \frac{1}{2}\vec{b}_t\Delta t^2 + \frac{1}{6}\vec{c}_t\Delta t^3 \\
\vec{a}_{t+\Delta t,p} &= \vec{a}_t + \vec{b}_t\Delta t + \frac{1}{2}\vec{c}_t\Delta t^2 \\
\vec{b}_{t+\Delta t,p} &= \vec{b}_t + \vec{c}_t\Delta t \\
\vec{c}_{t+\Delta t,p} &= \vec{c}_t.
\end{aligned}
\tag{39}
$$

The first and second derivatives of the acceleration in Eq. (39) depend on the order of the Gear scheme used. For the third (GPC3) and fourth order (GPC4) Gear predictor corrector algorithms they are calculated as $\vec{b}_t = d\vec{a}/dt, \vec{c}_t = 0$ and $\vec{b}_t = d\vec{a}/dt, \vec{c}_t = d\vec{b}/dt$, respectively. Finally, the predictor results are used to calculate the positions and their higher derivatives as

$$\begin{aligned}
\vec{r}_{t+\Delta t} &= \vec{r}_{t+\Delta t,p} + v_1 \Delta \vec{a} \Delta t^2 \\
\vec{v}_{t+\Delta t} &= \vec{v}_{t+\Delta t,p} + v_2 \Delta \vec{a} \Delta t \\
\vec{a}_{t+\Delta t} &= \vec{a}_{t+\Delta t,p} + v_3 \Delta \vec{a} \\
\vec{b}_{t+\Delta t} &= \vec{b}_{t+\Delta t,p} v_4 \frac{\Delta \vec{a}}{\Delta t} \\
\vec{c}_{t+\Delta t} &= \vec{c}_{t+\Delta t} + v_5 \frac{\Delta \vec{a}}{\Delta t^2},
\end{aligned} \tag{40}$$

where $\Delta \vec{a} = \vec{a}_{t+\Delta t} - \vec{a}_{t+\Delta t,p}$ and the values for $v_1 - v_5$ are listed in Table 2. Only third and fourth order Gear scheme parameters are presented in Table 2 but higher order schemes also exist. Gear's schemes are highly accurate and are used in many applications (Balevičius et al. 2006; Peters et al. 2005; Behera et al. 2005; Thompson and Grest 1991).

TABLE 2   Gear Predictor corrector algorithm parameters $v_1 - v_5$

Scheme	v_1	v_2	v_3	v_4	v_5
GPC3	1/12	5/12	1	1	0
GPC4	19/240	3/8	1	3/2	1

There is no simple rule for choosing an appropriate time integration scheme. The higher order schemes have higher computational costs per time step but usually they can be used with longer time steps, which decreases the amount of total calculations. A typical criterion for the size of the time step states that the collision time of two particles should be long compared to the time step size. Often a ratio of 100 is used. The choice of integration scheme should be made for each application specifically. Many times such a systematic and laborious evaluation of each scheme is not possible and an educated guess has to be made. To back up the choosing process, studies where different schemes are compared can be explored (Kruggel-Emden et al. 2011, 2008; Rougier et al. 2004; Fraige and Langston 2004).

2.6   Generation of the simulation lattice

In the preceding sections all the necessary components for a discrete element simulation of granular materials are presented. For a granular flow simulation, the particles can be given a random and loose non-overlapping starting geometry using several methods not presented here. Instead, we will focus on approaches to produce different kinds of starting configurations for densely packed granular materials. Together with the cohesive interactions of section 2.4, these starting

configurations can be used to study solid materials. The methods can be roughly divided into static and dynamic methods. In static methods, the particles are given starting locations based on predescribed geometrical arrangement. In dynamic methods, the time integration schemes presented earlier are used together with appropriate body forces to arrive at the desired configuration. In Fig. 11 three different simulation lattices produced with static methods are shown. The lattices are easy to produce because the coordinates of each sphere results from exact mathematical formula. With this method very large lattices can be produced with very small computational cost. All lattices in Fig. 11 are produced with equal sized disks or spheres but polydisperse particles can also be used. For example, the interstitial sites of regular packings can be filled with smaller particles.

(a)   (b)   (c)
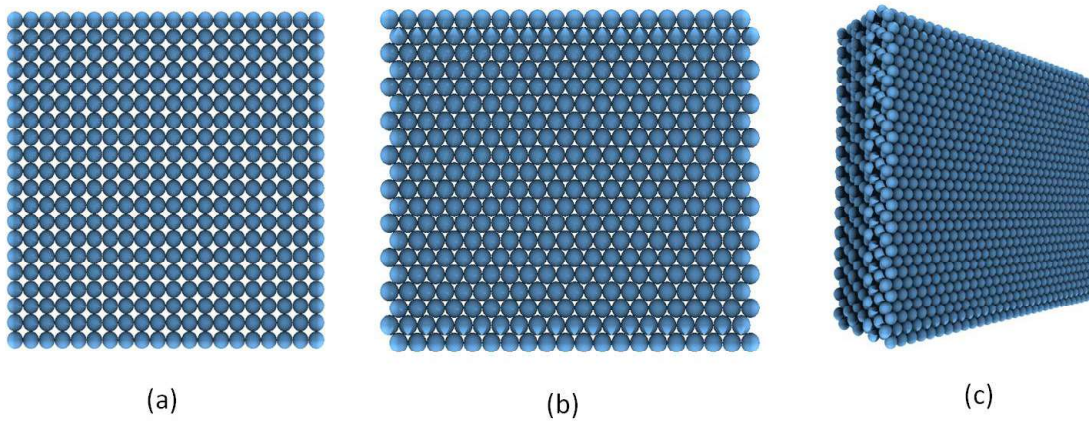
FIGURE 11   Two-dimensional (a) cubical and (b) hexagonal and three-dimensional (c) face-centred-cubic (Elliot 2000) packing arrangements.

The problem with the arrangements shown is that the material that the model tries to simulate becomes highly anisotropic. For example, when fracture and fragmentation of brittle materials is simulated, the fracture surfaces have a tendency to follow the surfaces induced by the regular packing. To remedy this shortcoming for static lattice generation methods, one can use mesh generation programs that rely on triangulation algorithms like Delaunay triangulation (de Berg et al. 2008). In Fig. 12 the mesh generated by a program called Netgen is shown together with a discrete element lattice produced based on the mesh. The lattice is produced by placing a sphere in each vertex of the mesh. In the generation of the lattice monodisperse particles are used, but a tighter packing could be achieved by increasing the sphere sizes in each location as long as the particles do not overlap.

The dynamic method presented is a simple sedimentation scheme used in many applications (Wiącek and Molenda 2014; Rubio-Largo et al. 2015; Pál et al. 2014). The idea in the method is that the particles are first arranged in a relatively loose vertical column above a container of desired shape. After that, gravity or similar body force is applied to the particles and the system is driven forward
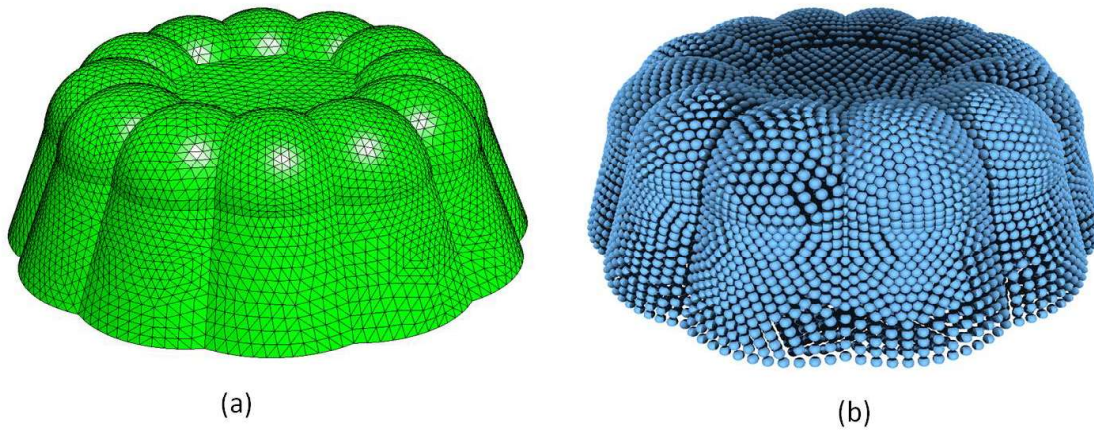
FIGURE 12   Triangular mesh generated with Netgen program (a) and a sphere lattice
               for the use of DEM simulation (b) based on the Netgen mesh.

with the force and time integration schemes presented in the earlier sections. The
dissipative force terms allow for dissipation of energy. Finally the system of par-
ticles lies in a dense random packed form in the bottom of the container. In this
approach the particles can be made polydisperse and it is actually recommended
if isotropic lattice is desired. The monodisperse collection will have a tendency
to pile up in a regular lattice which once again creates anisotropic behaviour. The
buildup of a sedimented granular lattice is illustrated in the image series of Fig.
13.
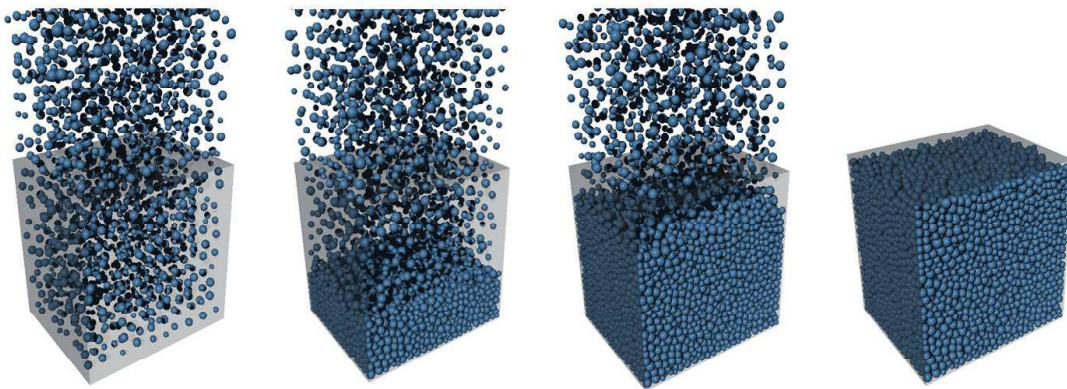
FIGURE 13   Four time steps of a dynamic sedimentation lattice generation simulation

Another dynamic method widely used is very similar to the sedimentation type
of lattice generation. Here, a similar initial configuration of loose particle pack-
ing is used. In this case, the particles can be scattered evenly in every direction
around a desired centre point. Next, a centripetal force that drives all the parti-
cles to the direction of centre point is induced. Once again the damping dissipates
kinetic energy and the resulting geometry has a spherical shape. Further geomet-
rical restrictions can be applied to remove particles from the acquired spherical

aggregate to yield desired lattice shapes.

So far the general guidelines of building a typical DEM model has been presented but no attention is paid on how to describe a specific material within the DEM framework. In the next chapter, a specific DEM application is presented where the model description and simulation parameters are chosen to yield specific material behaviour. With the acquired model, some numerical experiments are performed to validate the model and to gain insight into some glacier-related problems.

3 GLACIER DEM

3.1 Glacier ice

Ice has 18 different crystal structures and three amorphous states (Chaplin 2016). The form that exists under the typical temperature and pressure conditions of glaciers and ice sheets is termed as ice Ih (Greve and Heinz 2009). The letter h stands for hexagonal because water molecules in this type of crystalline form are arranged in layers of hexagonal rings. The hexagonal plane is referred to as the basal plane and perpendicular to this plane is the optic axis or c-axis (see Fig. 14 (a)).
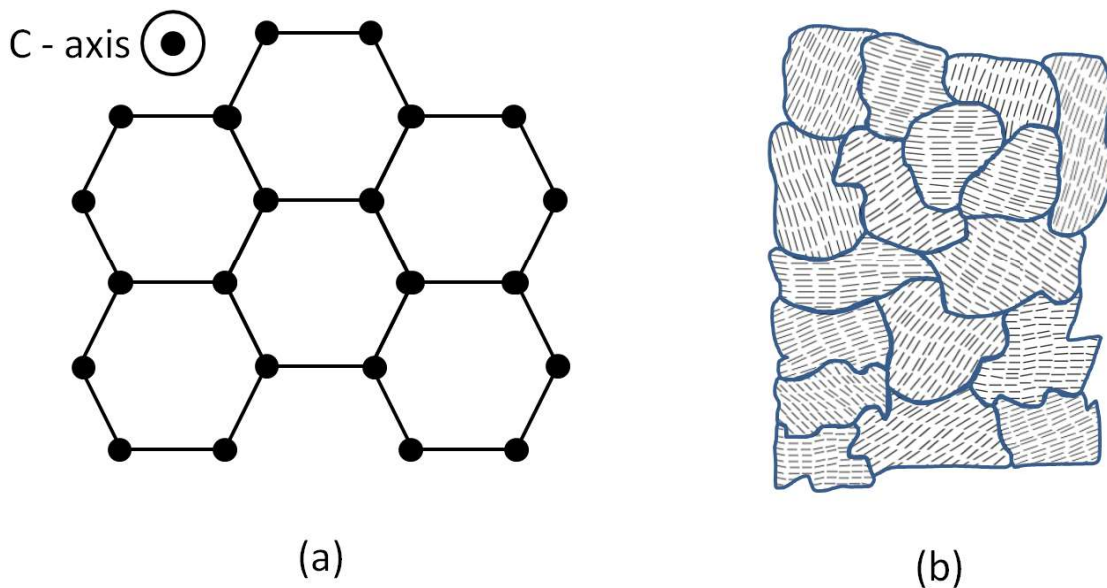

(a)   (b)

FIGURE 14   Ice at different scales. (a) Crystal hexagonal structure of ice Ih and (b) poly-crystalline ice formed from distinct ice crystals. In (a) the circles represent oxygen atoms of H_2O molecules and in (b) the lines represent directions of c-axes.

As one might expect, the elastic and brittle properties of the hexagonal crystal structure are highly anisotropic. The Young's modulus is highest when measured in the direction of the c-axis and uniaxial tensile strength is strongest when load is applied perpendicular to it (Schulson and Duval 2009). Such direction specific properties would require a quite complicated DEM model but fortunately large ice masses do not occur in single crystals but as an aggregate of them i.e. as polycrystalline ice (see Fig. 14 (b)). Inside a single crystal of polycrystalline ice the c-axes are more or less oriented in the same direction (variations occur due to crystallographic defects) but in a large collection of randomly oriented crystals the anisotropy of single crystals is averaged out and the material becomes effectively isotropic. The typical size of crystals or grains is of sub-millimetre scale in freshly formed or highly deformed ice, to tens of centimetres in very old or slowly moving ice (Greve and Heinz 2009). In a glacier measured in hundreds of meters or kilometres the isotropy assumption is well justified.

Based on the above reasoning, the elastic properties of glacier ice can be described with only two independent constants chosen from Young's modulus Y, the shear modulus G, Poisson's ratio ν, the bulk modulus K and the Lamès first parameter λ (Sadd 2009). In our investigations we have chosen the Young's modulus, which is the ratio of stress along an axis to strain along that same axis, and the Poisson's ratio defined as the ratio of transverse strain to axial strain. The experimental values reported for glacier ice Y have relatively large scatter. Gammon et al. (1983) report a value as high as 9.33 GPa, while Weeks and Assur (1967) on the other hand report a scatter from 1.7 GPa to 9.1 GPa. In general, Young's modulus depends on temperature and brine volume as well as other more minor factors. It should also be noted that ice is not purely elastic material but also viscous, a fact that we will discuss more below. The important thing to realize is that the result of mechanical measurement of Young's modulus depends on the loading rate as the viscous effect comes into play. Therefore the reported values for Y acquired with mechanical methods should be used with caution. Instead, values acquired with measurements of propagation of elastic waves or ultrasonic methods should be preferred. A range of values for Y for homogeneous polycrystalline ice is shown in Table 3 together with other ice properties that will be discussed shortly. At this point, it is emphasized that ice is a highly diverse material and the properties listed in Table 3 depend greatly of numerous factors like temperature, salinity, porosity, microcrack density and so on. The parameters listed are used as general guidelines in the model formulation and should not be considered as constant material properties.

Poisson's ratio also has a large scatter depending on loading rate, temperature, grain size, state of microcracking etcetera (Timco and Weeks 2010). The value used often in literature is 0.325 reported by Gammon et al. (1983) for polycrystalline ice at $-16\,°C$. The range for ν in Table 3 is given based on the temperature correction function given in the same reference applied to temperature range $-50°C$ - $0°C$. It is noteworthy however that this range widens drastically if anisotropy in the ice is present (Schulson and Duval 2009).

According to Timco and Frederking (1996), based on a large number of ex-

TABLE 3 Ice properties

Property	Symbol	Unit	Value
Young's modulus	Y	Nm^{-2}	$(1-10) \cdot 10^9$
Poisson's ratio	ν	-	$0.309 - 0.332$
Density	ρ	$\mathrm{kg/m^3}$	$720 - 940$
Tensile strength	σ_t	MPa	$0.5 - 1.0$
Flexural strength	σ_f	MPa	$0.4 - 1.1$
Shear strength	σ_s	MPa	1.1
Compression strength	σ_c	MPa	$1.3 - 13.0$
Fracture toughness	K_{IC}	$\mathrm{kPam}^{1/2}$	$50 - 500$
Arrhenius factor	A	$\mathrm{s}^{-1}\mathrm{Pa}^{-3}$	$3.6 \cdot 10^{-27} - 4.9 \cdot 10^{-25}$

perimental measurements, the density of sea ice varies from 720 $\mathrm{kg/m^3}$ to 940 $\mathrm{kg/m^3}$ with an average of 910 $\mathrm{kg/m^3}$. There are variations due to brine and air volumes, temperature, water submersion and inaccurate measuring techniques. The tensile strength of sea ice given by Timco and Weeks (2010) is in the range from 0.5 MPa to 1.5 MPa. They report also lower values for first-year sea ice but the values for old ice are more appropriate for glacier ice. The flexural and shear strength of old ice also falls into the same range as tensile strength but according to Timco and Weeks (2010) there are no reported values available in the literature. Estimates based on Timco and Weeks (2010) are shown in Table 3. Compressive strength is, as is common for many materials, considerably higher than tensile strength. Richter-Menge et al. (1987) report values roughly in the range $(1.3 - 13.0)$ MPa depending on strain rate and temperature. Mode I fracture toughness of glacier ice based on 20 experiments conducted by Andrews (1985) is in the range $57 - 142$ $\mathrm{kPam}^{1/2}$. The effect of temperature is not however treated in that study and can have significant effect on the values. That can be seen from the experiments conducted by Liu and Miller (1979) who report fracture toughness values for fresh-water ice in the range $86 - 471$ $\mathrm{kPam}^{1/2}$. Based on these values a large range is presented in Table 3.

In addition to the brittle and elastic behaviour, ice has also a viscous regime where the ice mass slowly flows under applied pressure. The schematic presentation of ice flow behaviour is shown in Fig. 15. When a constant stress is applied on an ice sample, it results immediately in a reversible elastic deformation. If the stress is not released the ice starts to deform irreversibly. This behaviour can be divided into three flow regimes as shown in Fig. 15, the primary, secondary and tertiary creep. The secondary creep has been a subject of a large number of studies and a mathematical description for it has been given already over 60 years ago by Glen (1955). The law bears the name of its inventor and is thereby called the Glen's flow law and is presented in the form
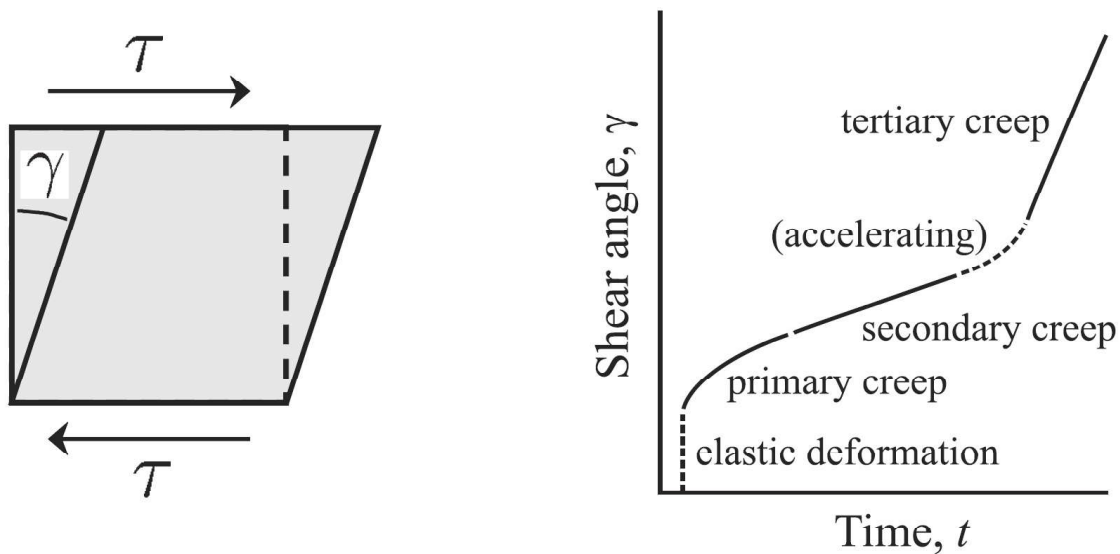
FIGURE 15   Shear behaviour of polycrystalline ice. The ice block is sheared with a constant shear stress τ and it results in shear angle γ in a time t (from Greve and Heinz (2009)).

$$\mathbf{D} = A(T)\sigma_e^{n-1}\mathbf{t}^D, \qquad (41)$$

where $A(T)$ is a temperature dependent Arrhenius factor, σ_e is the second invariant of the deviatoric stress tensor, $\mathbf{D}$ is the strain-rate tensor, $\mathbf{t^D}$ is the deviatoric stress tensor, and $n \approx 3$. The Arrhenius factor depends on the temperature and it varies from $3.6 \cdot 10^{-27}$ $\mathrm{s^{-1}Pa^{-3}}$ at $-50\,^\circ\mathrm{C}$ to $4.9 \cdot 10^{-25}$ $\mathrm{s^{-1}Pa^{-3}}$ at $-10\,^\circ\mathrm{C}$. Therefore the flow velocity of a glacier is highly dependent on the temperature.

3.2   DEM model for glacier dynamics

In Chapter 2, a brief description of discrete element methods and in Section 3.1, the properties of glacier ice were presented. Here, they are combined to yield a numerical model for glacier ice. The model consists of two-dimensional polydisperse collection of disks. The dispersion (range of disk sizes) was kept high enough to avoid crystallization but low enough to keep the computational cost relatively low. Based on numerical experiments, a good ratio between the largest and smallest diameters of the disks was found to be 1.33. The obvious difference in the isotropy between monodisperse and polydisperse collection can be seen in Fig. 16 (a) and (b). Since the goal was to simulate isotropic polycrystalline glacier ice, the polydisperse collection is favoured. Otherwise, the simulated material would be predisposed to fracture and deform in the direction of symmetric crystal orientations shown in Fig. 16 (a). The simulation lattices have been constructed with the sedimentation scheme explained in section 2.6. After the sedimentation simulation has come to rest, the possible beam connections are found

with Delaunay triangulation algorithm. A beam suggested by the triangulation is accepted as a beam if it connects disks that are close enough to each other. This acceptance condition is expressed in the form

$$d \leq C(r_1 + r_2),\tag{42}$$

where d is the distance between disks, C is a constant larger than unity, and r_1 and r_2 are radii of disks that are candidates to be connected. A choice $C = 1$ results in a low coordination number (average number of connecting beams for a single disk) of the lattice and therefore to a too weakly connected material. However, C cannot be very large ($C \leq 2$) because long connections generated by Delaunay triangulation at the edges of the lattice and also elsewhere can form connections between disks with an unconnected disk in between them (see Fig. 16 (b)).

(a)   (b)
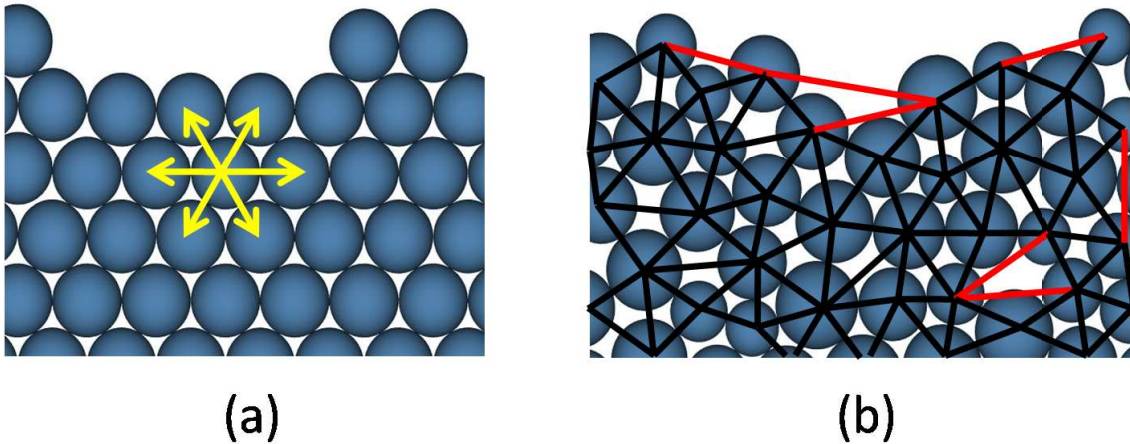
FIGURE 16   Monodisperse (a) and polydisperse (b) collection of disks. In (a), the yellow arrows represent symmetric crystal orientations and in (b), connections acquired from Delaunay triangulation algorithm are shown with lines. Red lines are not accepted as beams in the simulations.

The shear beam model presented in section 2.4.2 with small variations was used to calculate interactions between the disks. The formulation of the beam interactions starts with the elastic energy of a single beam,

$$E_{tot} = \frac{1}{2}k_s\epsilon^2 + \frac{1}{2}k_b(\theta_1^2 + \theta_2^2),\tag{43}$$

where ϵ, θ_1, and θ_2 are the axial strain and rotation angles of the two ends relative to the axis of the beam, respectively, and k_s and k_b are the corresponding stiffness parameters. Eq. (43) can be used to derive the forces and torques acting on the two ends of the beam in the form

$$
\begin{aligned}
\vec{f}_1 &= \frac{k_s \epsilon}{l_0} \hat{r} - \frac{k_b(\theta_1 + \theta_2)}{l} \hat{s}, \\
\vec{f}_2 &= -\frac{k_s \epsilon}{l_0} \hat{r} + \frac{k_b(\theta_1 + \theta_2)}{l} \hat{s}, \\
\vec{\tau}_1 &= k_b \vec{\theta}_1, \\
\vec{\tau}_2 &= k_b \vec{\theta}_2,
\end{aligned}
\tag{44}
$$

where l_0 and l are the equilibrium and deformed length of the beam, respectively. These equations are almost identical to Eq. (27) in section 2.4.2, but are slightly altered to match with Eq. (43). The unit vectors $\hat{r}$ and $\hat{s}$ have the same meaning as in Fig. 8. Deformation of the beam in the direction of the beam axis is damped by forces

$$
\vec{f}_1^{\mu} = s_\mu \dot{l} \hat{r}, \qquad \vec{f}_2^{\mu} = -s_\mu \dot{l} \hat{r},
\tag{45}
$$

and off-axis deformations are damped by torques

$$
\vec{\tau}_1^{\mu} = -b_\mu \dot{\vec{\theta}}_1, \qquad \vec{\tau}_2^{\mu} = -b_\mu \dot{\vec{\theta}}_2,
\tag{46}
$$

where dots represent time derivatives. Coefficients s_μ and b_μ are chosen to yield slightly underdamped deformation. When no mutual beam interaction exists between two disks, the repulsive part of the beam force is used as a contact potential to keep the disks from overlapping. The collisions are made inelastic with a similar damping term as associated with the axial beam force. A maximum value for beam elastic energy was chosen as a fracture criterion. Because $E \sim \sigma^2$, the fracture criterion can be identified as a Zhang and Eckert stress criterion (32). To allow for viscoelastic behaviour, the beams were allowed to break also before the energy threshold was reached with a stress dependent probability. Also, new beams were allowed to be formed between already disconnected disks. These fracture rules are explained in more detail in section 3.2.1. The forward Euler time integration scheme (34) presented in section 2.5 was used to drive the dynamics of the system forward. For repetition, the scheme for translational and rotational degrees of freedom can be expressed in the form

$$
\begin{aligned}
\vec{a}_i(t) &= \vec{F}_{tot}^i(t)/m_i \\
\vec{v}_i(t) &= \vec{v}_i(t - \Delta t) + \vec{a}_i(t)\Delta t \\
\vec{r}_i(t) &= \vec{r}_i(t - \Delta t) + \vec{v}_i(t)\Delta t
\end{aligned}
\tag{47}
$$

$$
\begin{aligned}
\vec{\alpha}_i(t) &= \vec{\tau}_i(t)/I_i \\
\vec{\omega}_i(t) &= \vec{\omega}_i(t - \Delta t) + \vec{\alpha}_i(t)\Delta t \\
\vec{\theta}_i(t) &= \vec{\theta}_i(t - \Delta t) + \vec{\omega}_i(t)\Delta t,
\end{aligned}
\tag{48}
$$

where $m_i = \pi \rho r_i^2$ is the mass of disk i with material density ρ and radius r_i. In Eqs. (47), $\vec{F}_{tot}^i$ is the sum of all forces acting on disk i, and $\vec{a}_i$, $\vec{v}_i$, and $\vec{r}_i$ are the acceleration, velocity, and position of disk i, respectively. Similarly in Eqs. (48),the

angular acceleration, angular velocity, and rotation angle of disk i are denoted by $\vec{\alpha}_i$, $\vec{\omega}_i$, and $\vec{\theta}_i$, respectively. The total torque acting on disk i is $\vec{\tau}_i$, and $I_i = \frac{1}{2}\pi\rho r_i^4$ is its moment of inertia. Time step Δt can be evaluated based on the resonance frequency of a simple harmonic oscillator given by $f_{res} = 1/(2\pi)\sqrt{k/m}$, where k is the spring constant for the oscillator and m the oscillating mass. The time step can be scaled as period of oscillation which is simply the reciprocal of frequency $\Delta t \sim T = 2\pi\sqrt{m/k}$. In two-dimensional system with unit depth the spring constant can be associated with Young's modulus Y of the material as $k \sim Y\pi r$ and m with the mass of a single disk as $m \sim \rho\pi r^2$. Thus, the time step Δt can be scaled as $\Delta t \sim \sqrt{\rho r/Y}$. Typical time step values in our simulations were in the range of $10^{-5} - 10^{-4}$ s.

3.2.1 Adjustment of elastic moduli

Owing to the polydispersity of the disks, the elastic properties of the model are heterogeneous and anisotropic in a scale comparable to the disk size. In larger scales, however, parameters k_s and k_b that control the beam stiffness can be chosen to yield desired Young's modulus and Poisson's ratio of the material in question. We start the derivation by considering an uniform two dimensional strain field in a lattice of points connected with beams. The deformation of a single beam in such a lattice is shown in Fig. 17.
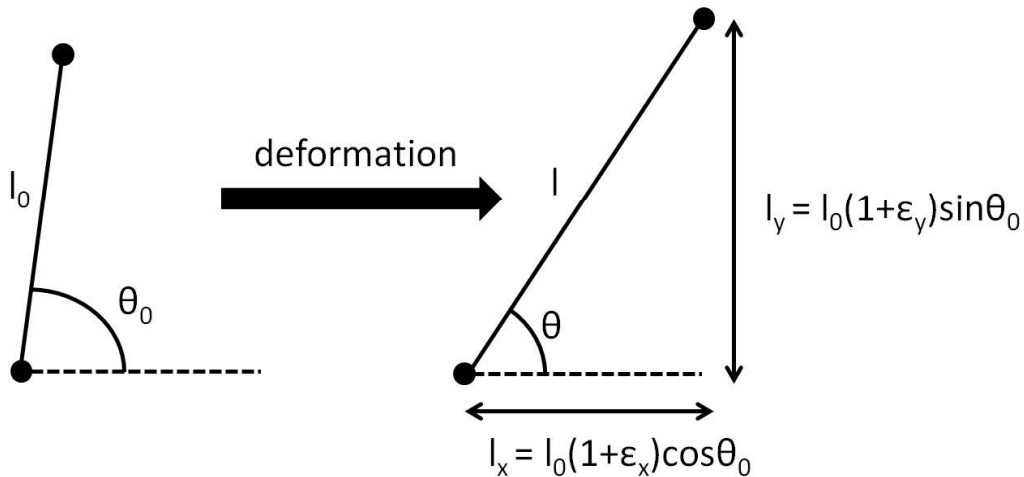
FIGURE 17   The configuration of a single beam in a uniform strain field before and after deformation.

The length l of the beam after the deformation as a function of its initial orientation angle θ_0 can be expressed as

$$l = \sqrt{l_x^2 + l_y^2} = \sqrt{l_o^2(1 + \epsilon_x)^2 \cos^2\theta_0 + l_0^2(1 + \epsilon_y)^2 \sin^2\theta_0}. \tag{49}$$

Because strains, especially for a brittle material like ice, can be assumed small $\epsilon_x^2 = \epsilon_y^2 \equiv 0$. Also, by using a trigonometric identity, $\sin^2\theta + \cos^2\theta = 1$, and a Taylor-series approximation, $\sqrt{1 + 2x} \approx 1 + x$, we find that

$$l \approx l_0(1 + \cos^2 \theta_0 \epsilon_x + \sin^2 \theta_0 \epsilon_y). \tag{50}$$

Thus the axial strain of the beam can be presented as

$$\epsilon = \frac{l - l_0}{l_0} \approx \cos^2 \theta_0 \epsilon_x + \sin^2 \theta_0 \epsilon_y. \tag{51}$$

The average strain energy of a beam can be calculated using Eq. (43) and integrating over all possible beam orientations,

$$
\begin{aligned}
u_s &= \frac{1}{\pi} \int_{-\pi/2}^{\pi/2} \frac{1}{2} k_s \epsilon^2 d\theta_0 \\
&\overset{\text{Eq.(51)}}{=} \frac{k_s}{2\pi} \int_{-\pi/2}^{\pi/2} \cos^4\theta_0 \, \epsilon_x^2 + 2\cos^2\theta_0 \sin^2\theta_0 \, \epsilon_x\epsilon_y + \sin^4\theta_0 \, \epsilon_y^2 \, d\theta_0 \\
&= \frac{k_s}{2\pi} \left(\frac{3\pi}{8} \epsilon_x^2 + \frac{\pi}{4} \epsilon_x\epsilon_y + \frac{3\pi}{8} \epsilon_y^2 \right) \\
&= \frac{k_s}{16} \left(3\epsilon_x^2 + 2\epsilon_x\epsilon_y + 3\epsilon_y^2 \right).
\end{aligned}
\tag{52}
$$

The average energy associated with rotational degree of freedom can be determined similarly. The angle θ can be expressed in the form

$$\theta = \tan^{-1}\left(\frac{l_y}{l_x}\right) = \tan^{-1}\left(\frac{l_0 \sin \theta_0 (1 + \epsilon_y)}{l_0 \cos \theta_0 (1 + \epsilon_x)}\right) = \tan^{-1}\left(\tan \theta_0 \frac{1 + \epsilon_y}{1 + \epsilon_x}\right). \tag{53}$$

The term on the right hand side of Eq. (53) can be further modified by treating $(1 + \epsilon_y)/(1 + \epsilon_x)$ as a variable and representing it as a Taylor series around point 1. This yields

$$\tan^{-1}\left(\tan \theta_0 \frac{1 + \epsilon_y}{1 + \epsilon_x}\right) \approx \theta_0 + \underbrace{\frac{\tan \theta_0}{1 + \tan^2 \theta_0}}_{\sin \theta_0 \cos \theta_0} \left(\frac{1 + \epsilon_y}{1 + \epsilon_x} - 1\right). \tag{54}$$

By combining Eqs. (53) and (54) we find that

$$\theta - \theta_0 = \Delta\theta = \sin \theta_0 \, \cos \theta_0 \left(\frac{1 + \epsilon_y}{1 + \epsilon_x} - 1\right). \tag{55}$$

As in the case of axial deformation, the average energy of rotations can then be calculated by integrating the beam energy over all possible beam orientations,

$$u_b = \frac{1}{\pi} \int_{-\pi/2}^{\pi/2} k_b \Delta\theta^2 d\theta_0$$

$$= \frac{k_b}{\pi} \left(\frac{1+\epsilon_y}{1+\epsilon_x} - 1\right)^2 \int_{-\pi/2}^{\pi/2} \sin^2\theta_0 \, \cos^2\theta_0 \, d\theta_0$$

$$\approx \frac{k_b}{8}(\epsilon_x - \epsilon_y)^2. \tag{56}$$

The last form is approximative since again the strains are assumed to be small in the derivation. In the case of brittle materials this condition is usually met. By adding Eqs. (56) and (52), multiplying by beam density ρ_b and rearranging gives the total strain energy density as

$$F = \rho_b \left(\frac{k_s}{8} + \frac{k_b}{4}\right)(\epsilon_x^2 + \epsilon_y^2)$$

$$+ \rho_b \left(\frac{k_s}{16} - \frac{k_b}{8}\right)(\epsilon_x^2 + 2\epsilon_x\epsilon_y + \epsilon_y^2). \tag{57}$$

The beam density $\rho_b = c_C/r^2$ is the number of beams per unit area. The parameter c_C depends on the beam length parameter of Eq. (42) and r is the average beam size. Eq. (57) serves now as a tool to couple the simulation parameters to elastic parameters of a real material. This is done by comparing Eq. (57) to continuum strain energy of the plain-strain deformation (Landau 1970),

$$F = \frac{Y}{2(1+\nu)}(\epsilon_x^2 + \epsilon_y^2)$$

$$+ \frac{Y\nu}{2(1+\nu)(1-2\nu)}(\epsilon_x^2 + 2\epsilon_x\epsilon_y + \epsilon_y^2). \tag{58}$$

From Eqs.(57) and (58) we find that

$$Y = \rho_b \frac{5k_s^2 + 8k_bk_s - 4k_b^2}{16k_s} \tag{59}$$

and

$$\nu = \frac{1}{4} - \frac{k_b}{2k_s}. \tag{60}$$

To test if the coupling presented above satisfactorily induces realistic elastic properties for the simulation model, a test simulation setup was investigated. A 45 m × 45 m material block of 17570 disks with uniform size distribution between 0.3 m and 0.4 m was constructed. The right edge of the lattice was held in place in the x-direction and a tensile stress of 100 kPa was applied to the left edge. The

stress was applied only in x-direction. Thus, a vanishing stress in y-direction can be required, yielding

$$\sigma_y = \frac{\partial F}{\partial \epsilon_y} = 0. \tag{61}$$

By substituting Eg. (58) to Eq. (61) we get for the strain ratio

$$\frac{\epsilon_y}{\epsilon_x} = \frac{\nu}{-1 + \nu}. \tag{62}$$

In a similar way, the stress in the x-direction can be solved as a partial derivative of F with respect to ϵ_x to find

$$\sigma_x = \frac{\partial F}{\partial \epsilon_x} = \frac{Y}{1 + \nu} \left(\epsilon_x + \frac{\nu(\epsilon_x + \epsilon_y)}{1 - 2\nu} \right). \tag{63}$$

Substitution of Eq. (62) into Eq. (63) and rearrangement gives

$$Y = \frac{\sigma_x}{\epsilon_x}(1 - \nu^2). \tag{64}$$

By using glacier ice properties guided by Table 3, we can test how well the model is able to reproduce the desired material properties. The values chosen for elastic parameters are $Y = 5$ GPa and $\nu = 0.2$. Notice a value of ν a little lower than typical for glacier ice (Table 3). This choice has been dictated by model description because Eq. (60) can not produce values higher than 0.25 with any choice of k_s and k_b. Values relatively close to glacier ice can still be achieved. In Fig. 18 values for Y and ν derived straight from the simulations are shown as functions of relative beam length C.
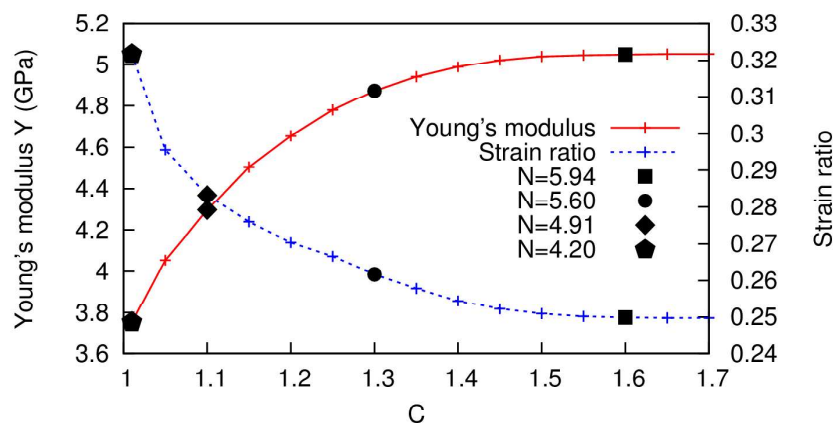
FIGURE 18   Effect of maximum relative beam creation length C, defined in Eq. (42), on the elastic properties of a 17570-disk lattice. Expected value for the strain ratio was 0.25 corresponding to a Poisson's ratio of $\nu = 0.2$ (see Eqs. (60) and (62)), and the expected value for the Young's modulus was $Y = 5.0$ GPa (Eq. 59). The values of the coordination number, N, are shown for some values of C. (Modified from paper II Fig. 5.)

It can be seen from the results that the parameter C strongly controls the elastic properties of the material. With a value of $C = 1.01$ we get 30 % deviations from the accurate values but with a choice of $C = 1.6$ the deviations drop down to roughly 1 %. The deviation is induced by nonaffine deformations in the low C limit that result from low values of coordination number N (see Fig. 18). An plausible description of elastic properties can thus be obtained by using a sufficently high value of parameter C.

3.2.2 Adjustment of fracture properties

The fracture properties were studied with energy considerations in a quasistatic simulation setup. In the model, fracture energy per unit length, G_c, includes the deformation energy of broken beams along the crack given by Eq. (43). This energy density can be approximated as $\sqrt{\rho_b} E_c$, where E_c is the critical fracture energy of the beam. Energy is also dissipated in the surroundings of the broken beams, the amount of which is comparable to the elastic energy of the beam. With the above reasoning, we can state the breaking limit of a beam in the form

$$E_c = c_f \frac{G_c}{\sqrt{\rho_b}}, \tag{65}$$

where c_f is a constant that accounts for the energy sinks mentioned above, and can be found from simulations presented below. The simulation setup consisted of an edge cracked material block which was stressed in the direction perpendicular to the crack surface (see Fig. 19 (a)). The physical size of the simulated block was 30×60 m^2 and it consisted of 15543 disks with an average diameter of 0.35 m. The elastic properties were selected as in the previous chapter and $E_c \approx 2$ J. The beam density was roughly 26 beams/m^2.

According to Zehnder (2012), the critical energy release rate G_c for a plane-strain situation is

$$G_c = \frac{K_{IC}^2 (1 - \nu^2)}{Y}. \tag{66}$$

The critical stress intensity factor K_{IC} on the other hand can be presented for an edge cracked specimen with dimensions of Fig. 19 (a) in the form (Hertzberg 1996)

$$K_{IC} = \sigma_c \sqrt{a} \overbrace{\left[1.99 - 0.41(\frac{a}{W}) + 18.7(\frac{a}{W})^2 - 38.48(\frac{a}{W})^3 + 53.85(\frac{a}{W})^4 \right]}^{\equiv B}, \tag{67}$$

where a and W are the length of the edge crack and the width of the specimen, respectively. By combining Eqs. (66) and (67) and rearranging we get

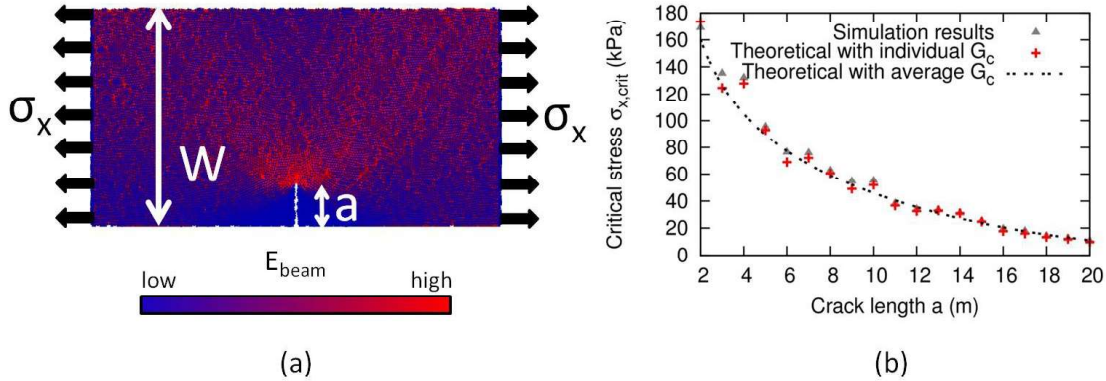$$\sigma_c = \sqrt{\frac{G_c Y}{a(1 - \nu^2)B^2}}. \tag{68}$$

FIGURE 19   (a) The simulation setup for studying the fracture properties of the model. Stress intensity is visualized by showing the elastic energy E_{beam} of individual beams. (b) The critical stress as a function of initial crack length. Simulated values together with theoretical predictions are shown. (Modified from paper II Fig. 6)

The stress σ_x was slowly increased in the simulation setup until a catastrophic failure occurred. The stress at this point was recorded and the values as a function of crack length are plotted in Fig. 19 (b). For each crack length the values for G_c were determined from the simulations and together with Eq. (68) the theoretical values for critical stress were obtained. In principle, the values for G_c do not depend on crack length, however the granular nature of the simulation lattice creates small variations. In Fig. 19 (b), the theoretical values for σ_c with individual values of G_c and a curve with average $G_{c,av} \approx 42$ J/m are shown. Based on $G_{c,av}$, the value of c_f in Eq. (65) is roughly $c_f \approx 0.24$. Fracture toughness can be estimated based on the average value of strain energy release rate $G_{c,av}$ by using Eq. (66) to yield $K_{IC} \approx 468$ kPam$^{1/2}$. The value is relatively high but in the range given in Table 3. The adjustment of fracture properties was restricted to the case of fracture toughness but tensile, flexural, shear and compression strengths of ice could also be adjusted through simulation parameters to yield values listed in Table 3.

Another test to see if the model material exhibits realistic brittle behaviour is to study the fragment size distributions (FSD) of fragmentation events. A simple simulation setup was constructed where a material block was subjected to a uniform 10 kN radial-inflation force field. According to Åström (2006), Åström et al. (2000) and Kekäläinen et al. (2007), FSD of a fragmentation process can be expressed in the form

$$n(s) \propto (1 - \beta)s^{-\alpha} \exp(-(2/w)^D s) + \beta \exp(-s_0^{-1}(s^{1/D}w)^D), \qquad (69)$$

where n is the number of fragments of size s. The first part of the distribution originates from the fragments formed within the damage zones around the paths of the propagating main cracks, and the second part corresponds to merging of

these main cracks. The relative normalization of the two parts of the distribution is controlled by parameter β, $\alpha = (2D - 1)/D$ with D the spatial dimension of the space (here $D = 2$), w is the width of the damage zones, and s_0 represents the typical size of large fragments formed by merging of main cracks. In the simulations, a material block constructed from 13902 disks was used. The physical size of the block was $100 \times 100 \text{ m}^2$. Other parameters were $Y = 0.1$ GPa, $\nu = 0.2$, and $G_c \approx 800$ J/m. Two simulations were conducted with different values of damping parameters s_μ and b_μ. The damping parameters affect the crack branching and therefore influence the form of the FSD curve. With weak damping ($s_\mu \approx 100 \text{ Ns/m}^2$ and $b_\mu \approx 10 \text{ Ns/m}^2$), the crack branches can propagate far from the main cracks and large damage zones can be formed (see Fig. 20 top).
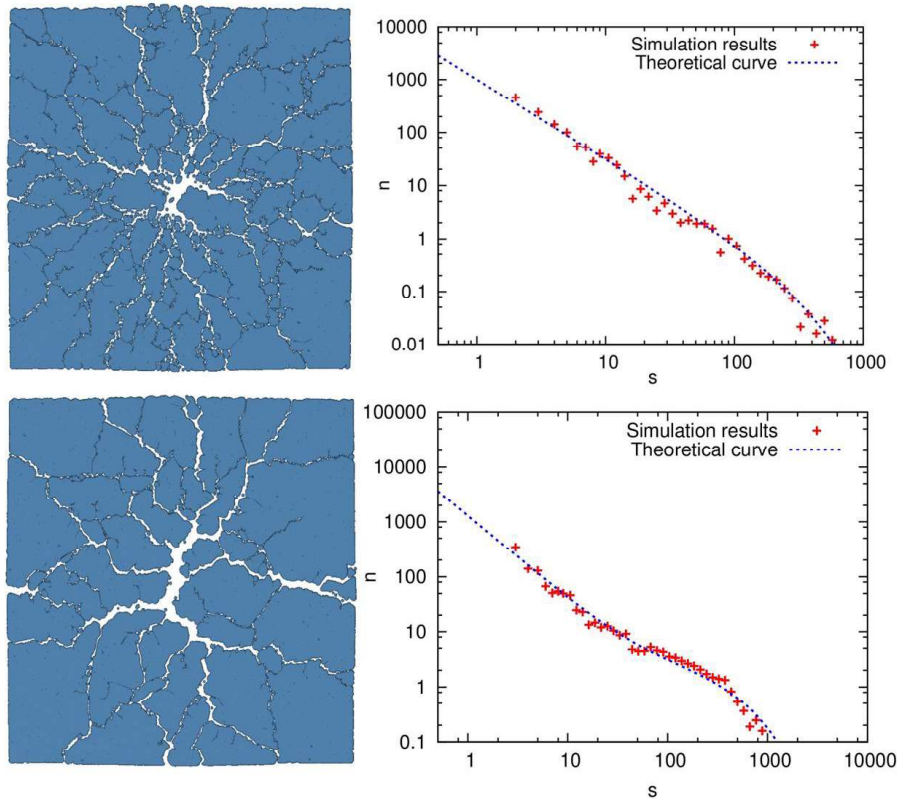
FIGURE 20   The top row displays a simulation result with a minimal damping together with the corresponding FSD. The dashed line is a fit by Eq.(69). The corresponding figures for the case of high damping are shown below these. (From paper II Fig. 8.)

With strong damping ($s_\mu \approx 10000 \text{ Ns/m}^2$ and $b_\mu \approx 1000 \text{ Ns/m}^2$) the side branches quickly die out and the fragmentation process is dominated by the main cracks (Fig. 20 bottom). It is clearly seen from Fig. 20 that the simulation model is able to reproduce the theoretically predicted behaviour of fragmenting bodies and that simulation parameters can be used to alter this behaviour for fragmentation of different kinds of materials.

3.2.3 Viscous behaviour

Two different mechanisms produce viscosity in our simulation model. The first one is related to damping of elastic beams. To damp elastic vibrations quickly, the damping parameters (Eqs. (45, 46)) should be chosen close to their critical values,

$$
\begin{aligned}
s_\mu^{crit} &\approx 2r\sqrt{\rho Y} \\
b_\mu^{crit} &\approx 2r^3\sqrt{\rho Y},
\end{aligned}
\tag{70}
$$

which can be derived from properties of the simulated system and from the theory of simple harmonic oscillators. The damping parameters were chosen slightly below the values given by Eq. (70) to yield weakly subcritical damping of beams. The second mechanism, contrary to beam damping, allows the material to deform irreversibly. It involves two new rules for beams: 1) Beams are allowed to break before the breaking threshold has been reached and 2) new beams can be formed between disconnected disks. If the probabilities for such events have suitable stress-dependency, the material is able to flow according to Glen's flow law (Eq. (41)). The scaling analysis is started by assuming that melting events are random and uncorrelated, which implies a probability $P_m = 1 - e^{-\lambda_m \Delta t}$ for a beam to break (melt) during time step Δt, where λ_m is the melting rate (melting events per second). Each broken beam is associated with relaxation of its elastic strain, $\epsilon \sim \sigma/Y$. Here σ approximates the stress in the beam. Thus, the strain rate of the simulated material can be expressed as $\dot{\epsilon} \sim \lambda_m \sigma/Y$. By choosing $\lambda_m = AY\sigma^{n-1}$, we obtain $\dot{\epsilon} \sim A\sigma^{n-1}\sigma$ which is similar to the tensorial form of Glen's law, Eq. (41) since $\sigma \sim t^D$. Because the elastic energy, E, of the beam is the elastic-energy density ($\sim \sigma^2/Y$) multiplied by the effective volume of the beam ($\sim r^2$), i.e., $E \sim \sigma^2 r^2/Y$, we find the melting rate, $\lambda_m = c_\lambda AY\sqrt{EY/r^2}^{n-1}$, in terms of the energy of the beam. In particular, $\lambda_m = c_\lambda AY^2E/r^2$ for $n = 3$. Correspondingly, the dynamic viscosity is given by $\mu \sim \frac{Y}{\lambda_m} \sim \frac{1}{A\sigma^2}$. The coefficient c_λ can be obtained from simulations.

In addition to the melting rule, a refreezing probability $P_f = 1 - e^{-\lambda_f \Delta t}$ is used, where Δt is length of one time step and λ_f is the freezing rate. Refreezing, implemented in the simulation by creation of a new beam between two disks, can take place if the requirement of Eq. (42) is fulfilled. This means that new beams may be formed between disks that are not strictly in contact. If refreezing is applied only between disks that are compressed against each other, the coordination number would reduce, and the material would slowly degrade. The current rule allows the material to undergo viscous flow such that the lattice retains its average coordination number.

We select the rate of refreezing so that it is slow compared to dynamic crack propagation, but fast compared to the melting rate, i.e., $\lambda_f \gg \lambda_m$, which means that the viscous flow rate is determined dominantly by the melting rate. If a beam is under compression, only its bending deformation energy can break it. This, together with the elastic repulsions between the disks, makes the viscous flow essentially incompressible in agreement with the Glen's law.

A simple simulation setup was constructed to test the viscous properties of the model. A material block with same elastic properties as before, but added with viscous properties presented above, was constructed. The right wall of the material block was made rigid and a constant shear stress was applied to the left wall (see inset of Fig. 21).
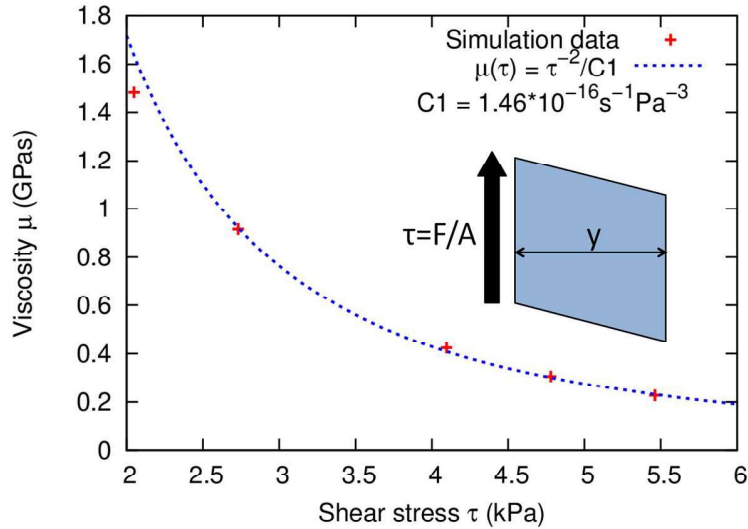

FIGURE 21   Simulation results for viscosity as a function of shear stress. The fitted curve (dotted line) is Glen's flow law. (From paper II Fig. 7.). In the inset, a schematic illustration of the simulation setup for investigating the viscous behaviour is shown.

Five different shear stresses were used and for each case the viscosity was calculated from

$$\mu = \frac{\tau}{D} = \frac{F/A_c}{u/y} = \frac{Fy}{A_c u}, \tag{71}$$

where τ is the shear stress, D is the strain rate, F is the shear force, A_c is the cross-sectional area of the block (unit width times height in this case), u is the shear velocity, and y is the distance between the sheared and rigid edges. The results of viscosity as a function of shear stress are shown in Fig. 21. As can be seen, the results are consistent with the behaviour described by Glen's flow law. The Arrhenius factor in these simulations was in the order of 10^{-17} s^{-1}Pa^{-3} which is many orders of magnitude larger than for ice at $-10°$C (Table 3). This choice of lower viscosity has been dictated by the restrictions of DEM models. The time step can not be made very large to keep the simulations stable. Therefore, the realistic time scale of glacier flow can not be reached. This is not necessarily a serious problem, however, because the time scales of viscous deformation and brittle fracture are still well separated even though viscous flow is speeded up.

4 GLACIER SIMULATION RESULTS

4.1 Calving of glacier ice

Glacier ice has been numerically studied almost exclusively by continuum methods, which treat ice as a continuous material with uniform or smoothly varying properties. Fracturing, however, is not continuous and the continuum models take into account the effects of fracturing through simple parameters such as depth of fracture penetration (Benn et al. 2007a,b; Nick et al. 2010), bulk "damage" (Jouvet et al. 2011; Borstad et al. 2012) or ice softness (Vieli et al. 2006). Even though these approaches are useful for many purposes, they are limited to be used only in certain kinds of continuous glacier simulations. Glacier calving, for example, is a highly discontinuous process which can be simulated in a straightforward and natural way with a DEM model. A better understanding of glacier calving is important because a large proportion $(40 - 50 \, \%)$ of mass loss in marine terminating ice fronts results from calving (Burgess et al. 2005; Walter et al. 2010; Depoorter et al. 2013). Thus, it has a major impact to the rise of sea level in the following decades and centuries.

Calving processes were studied extensively in our papers I, II and III. The method used in paper II is presented here in detail and from the other papers only the results are shown. The simulation setup consisted of a 100 m high ice block formed of 13902 disks (Fig. 22 (a)) resting on a slightly inclined plane. Water level at the front of the block was 80 m high and and gravity which caused a downward acceleration of 9.8 m/s^2, was applied. The water was simulated only as a simple buoyancy force for disks whose centres were below the water level. Other relevant parameters were $Y = 5 \, \text{GPa}$, $\nu = 0.2$, and $G_c \approx 970 \, \text{J/m}$ ($k_s \approx 3.4 \cdot 10^8 \, \text{J}$, $k_b \approx 3.4 \cdot 10^7 \, \text{J}$, $s_\mu \approx 8.0 \cdot 10^5 \, \text{Ns/m}^2$, $b_\mu \approx 8.0 \cdot 10^3 \, \text{Ns/m}^2$, and $E_c \approx 120 \, \text{J}$). It is important to notice that higher values of fracture energy, E_c, were used in the dynamic fragmentation simulations compared to the quasi-static case described in section 3.2.2. This is because the smallest fragments that can be formed in the simulations are single disks which are roughly one meter in size. In reality, the smallest fragments are typically of the grain size, which for glacier ice is of

the order of a few millimetres. Formation of a large quantity of millimetre-size fragments would demand a lot of crack-surface formation, which would absorb a vast amount of energy. To compensate for the missing energy sink, fracture energy, E_c, has to be increased in the simulations. Without this, nearly all the bonds would break and the material behaviour would more resemble sand than ice.
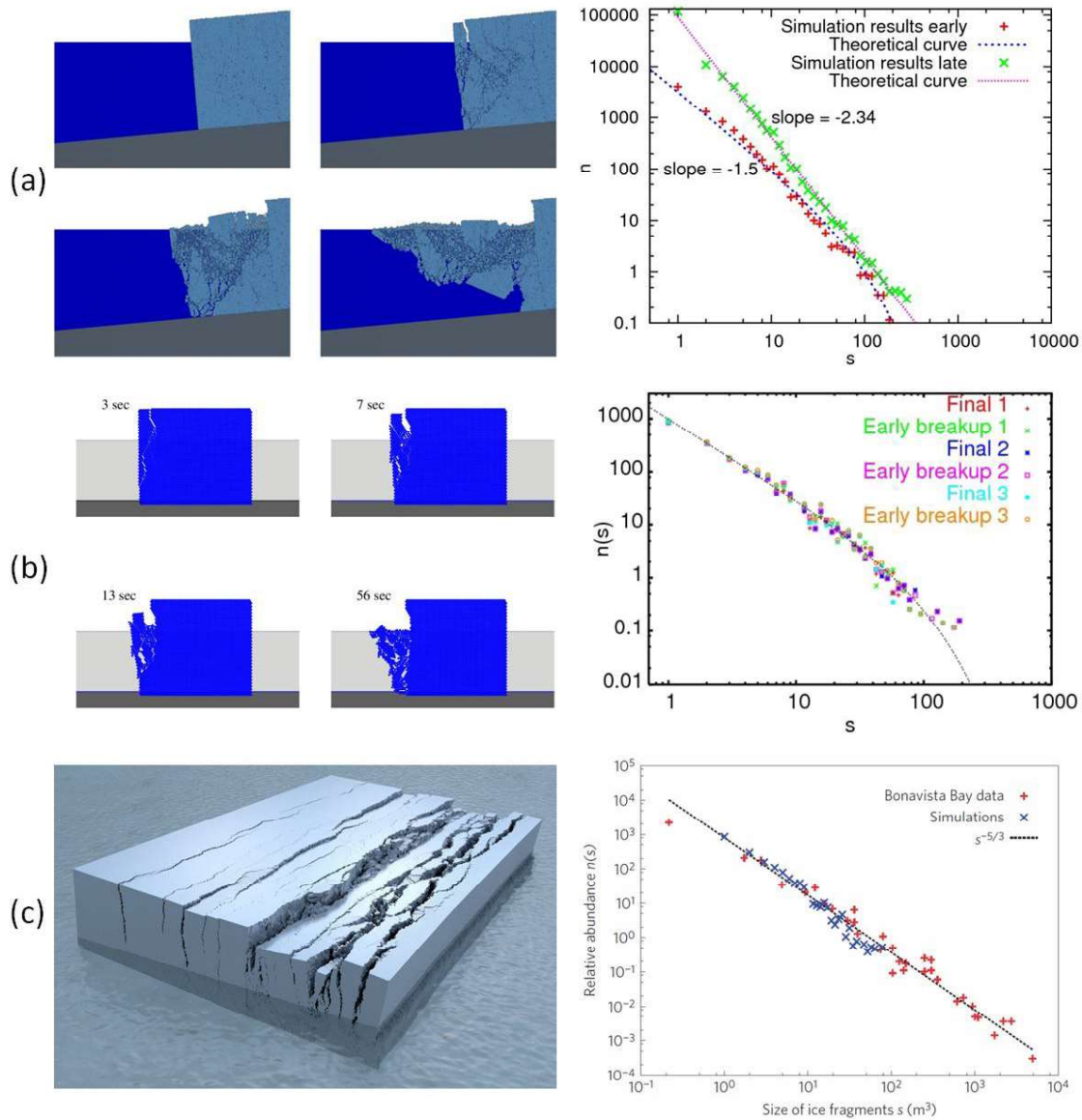
FIGURE 22   Snapshots of simulations and FSDs from the results of paper II (a), I (b) and III (c). The graphs in (a) and (b) show simulation results in early and late times of calving events together with theoretical curves. In (c) the results of simulations are compared to empirical findings from Bonavista Bay.

In Fig. 22 (a) a series of snapshots from these simulations are shown together with the FSDs required from early and late times of the simulation. In Fig. 22 (b) corresponding images from the results of paper I are shown. In that case a regular lattice like the one shown in Fig. 16 (a) was used. In Fig. 22 (c) the results of paper III

are shown where a three-dimensional lattice was used. The FSDs shown are from simulation results and also from experimental data acquired from chunks calved from icebergs in Bonavista Bay, Newfoundland. Each subplot in Fig. 22 has been fitted with Eq. (69) and for all of the cases except for the late moments of simulation (a) the power law exponent coincides with the value predicted by theory. The exception can be explained by the presence of grinding where subsequent collisions break the material into smaller pieces. Supported by experimental data and the majority of the simulations, one can propose that the FSD in glacier calving is usually formed in the initial breakup scenario and does not change significantly at later times. However, ice may become substantially weaker and more vulnerable to grinding when external conditions are favourable, for example in the vicinity of $0°C$ temperature. Also, glaciers that have a longer sub-aerial height are more prone to grinding because they have more potential energy that must be dissipated during a calving event until the system has come to rest.

4.2 Self-organized criticality of calving termini

In a calving event, ice fractures from glacier terminus when the strength of ice can no longer withstand the stress induced by its own weight. The propagating cracks trigger an ice 'avalanche' and a rapid burst of kinetic energy is observed together with corresponding loss of potential energy. Models describing such punctuated instabilities include the sandpile models, maybe the simplest systems that exhibit self-organized criticality (SOC). A distinguishing characteristic for SOC systems is the slow steady accumulation of instability which is followed by a fast relaxation through events of any possible size. For glacier calving, these events range from small local events that have insignificant effect on the overall shape of the terminus to system-wide collapse where the entire ice-cliff collapses. SOC systems have a sub-critical regime with infrequent and small events which leads to instability buildup over time. The other extreme is the super-critical regime where the instability relaxes through large events. They spontaneously self-organize towards a stable critical point between these two regimes. In the vicinity of this critical point, the system becomes scale invariant. For Abelian sandpile models (ASM), this behaviour is manifested as pure power laws for the mass distribution of avalanches $n(m) \propto m^{-\tau}$ and the waiting time distribution between consecutive avalanches $n(\delta) \propto \delta^{-\sigma}$. The exponents τ and σ are the critical exponents for each distribution.

To see if termini of calving glaciers can be considered as SOC systems, a broad experimental data set spanning 12 orders of magnitude in size was analysed from glaciers and ice shelves worldwide. The data sets were acquired from Svalbard, Alaska, Greenland and Antarctica with variety of methods. In Svalbard and Alaska, the data were collected by visual observations at the glacier terminus, by using seismographic methods and with time-lapse monitoring. In Greenland and Antarctica, satellite imaging was used. To back up the experimental results,
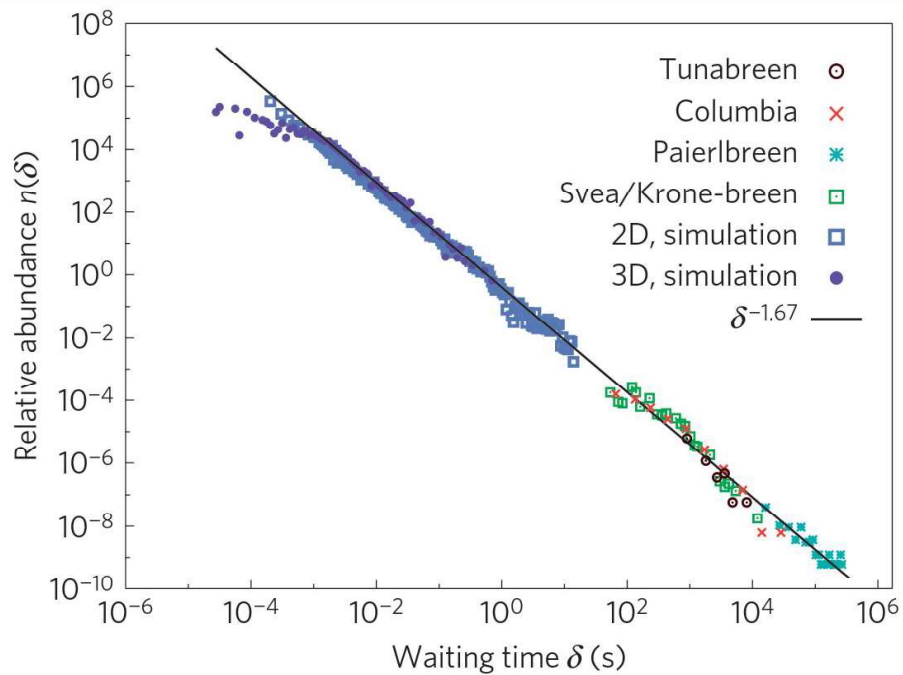
FIGURE 23 Waiting time distributions between consecutive calving events for Tunabreen, Paierlbreen, Kronebreen and Sveabreen Glaciers in Svalbard and Columbia Glacier in Alaska (Åström et al. 2014) together with simulation results in 2 and 3 dimensions. (From paper III Fig. 2 a)

simulations in 2 and 3 dimensions were conducted.

The first result indicative of SOC behaviour is the power law behaviour in waiting time distributions of calving events. Shown in Fig. 23 are the waiting time distributions from several glaciers in Svalbard and Alaska and simulation results from two- and three-dimensional implementations of the glacier DEM code. As is evident from the figure, the numerical and experimental waiting time distributions agree well with theory. The best-fit exponent for all data is $\sigma = 1.67 \pm 0.3$ which coincides well with ASM findings (Paczuski et al. 2005).

Secondly, SOC behaviour is backed up by the power law behaviour of calving volume (or equivalently mass) distributions. In Fig. 24 (a) the calving volume distributions for glaciers and ice shelves in Svalbard, Alaska, Greenland and Antarctica are shown. The data represents two distinct groups of relatively small and large calving volumes. The group with smaller calving volumes between 10^0 and 10^5 m^3 are grounded tidewater glaciers in Svalbard and Alaska and the group with volumes between 10^8 and 10^{12} m^3 are floating ice shelves in Antarctica and the large near-floating outlet glaciers in Greenland.

Both groups are reasonably well described by a power law with exponent $\tau = 1.2$ but the group with smaller calving volumes has an exponential cut-off at roughly 10^4 m^3. The exponential cut-off reflects the fact that the size of the calving event is limited by the physical size of the terminus of a grounded glacier. Bridging the gap between the two groups is the Columbia glacier during a transition from grounded to a floating terminus. This implies that grounded glaciers
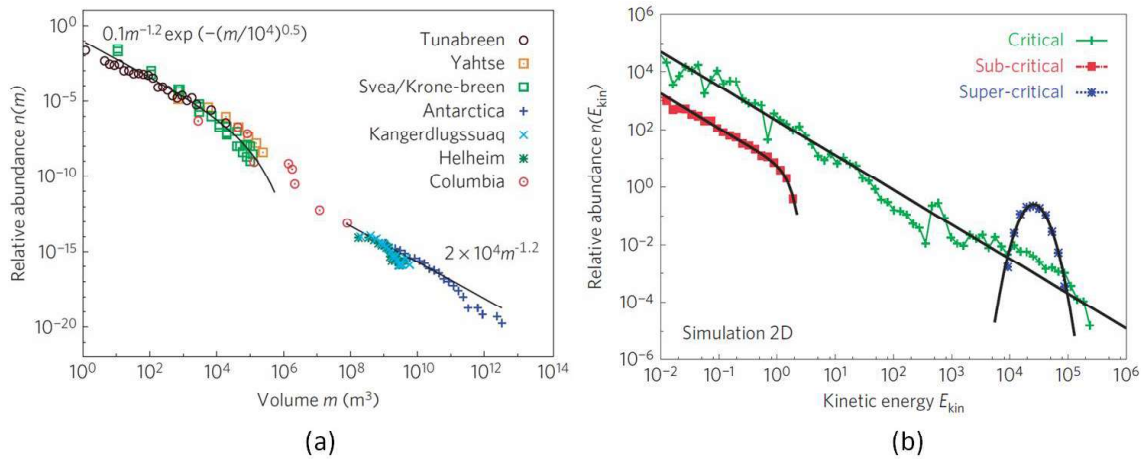
FIGURE 24   The calving volume distributions for (a) observed data and (b) simulated data with two-dimensional simulation model (From paper III Fig. 2 b and c).

are less prone to large scale events than floating ice shelves. By combining all calving volume data, a power law exponent of $\tau = 1.26 \pm 0.2$ is found, which is consistent with different variations of ASM (Dhar 1999, 2006).

The two-dimensional glacier DEM model was also used to study the calving volume distributions. In Fig. 24 (b) the distributions are shown for three different initial conditions. In these distributions the kinetic energy of a single event is used as a proxy for the amount of calved mass. The decision to use kinetic energy as opposed to mass directly is justified because the velocities of the calving particles have approximately the same range in any calving scenario and kinetic energy ($E_{kin} = 1/2mv^2$) is directly proportional to the mass and thus after rescaling approximates a similar distribution. Moreover, when comparing the simulation results to observed ones, a better comparison is achieved when only events with kinetic energy (i.e. non-zero velocity) are counted. This is because experimentally only detachment of ice mass from the glacier can be observed compared to simulations where a fragmented mass which has not calved can also be recorded. The critical fracture strain of a single beam was used as an adjustment parameter to yield different criticality regimes. As evident from Fig. 24 (b) the behaviour is distinctly different with varying initial conditions. In the sub-critical regime relatively small events occur and an exponential cut-off similar to that in observed data is seen. In the critical regime, large fluctuations and events ranging roughly 7 orders of magnitude are seen. The form of the distribution in this critical regime is approximated by a power law with exponent $\tau = 1.2$ and is thus consistent with observations. In the super-critical regime the distribution is dominated by large events and typically results in the failure of entire ice cliff in a single event. As expected for a SOC process, the event size distribution exhibits a pure power law in the critical point and distinctively different behaviours on either side of it.

Self organized criticality was further analysed by using a 3 dimensional version of the glacier ice simulation model. The initial conditions were varied
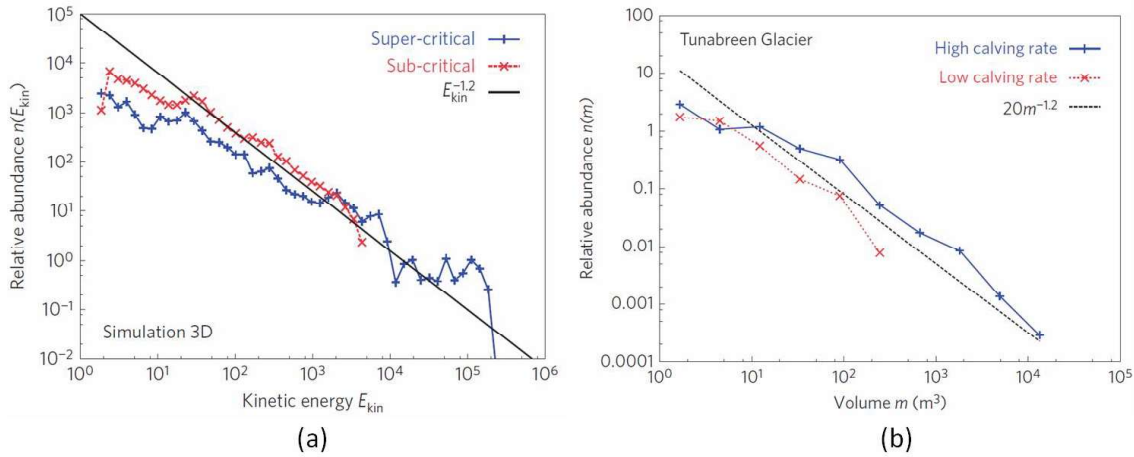
FIGURE 25 (a) The kinetic energy distribution of 3D simulation code with close to critical sub- and supercritical initial conditions and (b) distributions of calving event sizes in Tunabreen glacier observed in periods of high and low calving rate. (From paper III Fig. 2 and Fig. 3)

to yield near critical sub- and super-critical conditions. The resultant distributions for calving event sizes are shown in Fig. 25 (a), where the distributions approximatively follow a power law until the sub-critical distribution decays exponentially. The super-critical distribution on the other hand shows non-zero frequencies also for larger events. These distributions can be compared to the observations made in Tunabreen glacier. Tunabreen glacier is 100 m thick surging tidewater glacier subjected to local tidewater variations of less than 1 meter. Even though the tidal variation is a very small fraction of the glacier thickness, it has a strong influence on the calving rate at Tunabreen terminus. In the period of high tide the calving events are infrequent and small and in low tide they grow substantially in size and number thus resembling sub- and supercritical SOC regimes, respectively. In Fig. 25 (b) the event size distributions for these high and low calving rate regimes are shown which closely resemble results of Fig. 25 (a).

4.3 Viscous flow of glacier ice

To verify the flow behaviour of the glacier DEM model, its results were visually compared to ones given by the continuum ice model Elmer/Ice (Gagliardini et al. 2013; Gagliardini and Zwinger 2008; Zwinger and Moore 2009). In both simulation models, an ice block of size 30 m × 30 m was placed on a flat surface with little friction, and gravity was applied to drive the system forward. The state of the glacier DEM model in four different time steps is shown in Fig. 26 together with outlines from Elmer model for corresponding time intervals. As was pointed out earlier, the time step size in the DEM model cannot be made

large enough to reach the actual time scale of a deforming ice block or a glacier. Instead, the viscosity is made many orders of magnitude (in this case 10^5 times) lower than in real physical ice flow, and correspondingly higher strain rates are reached.
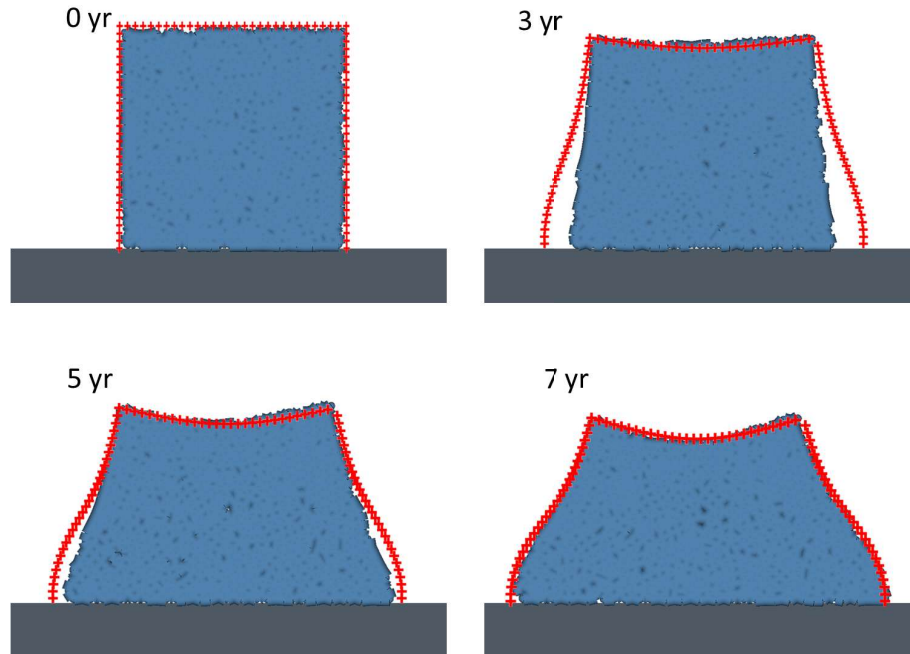

FIGURE 26   Snapshots of glacier DEM simulations with outlines from Elmer/Ice model (red markers). The time stamps refer to Elmer/Ice simulation model. In the glacier DEM model the time span is roughly 10^5 times shorter with correspondingly lower viscosity. (From paper I Fig. 5)

Even with this enhanced pace of flowing ice, the time scale of quickly propagating cracks is not reached and the two processes are kept well apart. As a proof of the validity of the model, the results shown in Fig. 26 closely resemble the Elmer/Ice results. The largest discrepancies can be seen in the early time steps, probably due to partial jamming of the granular material.

Another simulation setup was constructed to show that the model is capable of reproducing the analytical results given by shallow-ice equation. This equation gives the velocity of an ice sheet flowing down an inclined plane as a function of depth from the ice surface. It can be presented in the form (Lüthi 2013)

$$v_p(z) = \frac{2A}{n+1}(\rho g \sin \alpha)^n (H^{n+1} - (H-z)^{n+1}) + v_b, \tag{72}$$

where A and n are the Arrhenius factor and stress exponent of the Glen's flow law, respectively. Inclination angle of the plane is denoted by α, ρ is the mass density of ice, g the acceleration caused by gravity, H the height of the ice block, and v_b the depth dependent sliding velocity. The velocity profile was acquired from the middle part of a simulated down slope ice block from the area marked

with black thick lines in Fig. 27 (a). Equation (72) is formulated for an ice sheet of infinite width and length so an ice block with large aspect ratio (30 m × 200 m) was used and the values were acquired from the middle part to diminish the boundary effects. The results of the simulation are shown in Fig. 27 (b) and they follow the theoretical predictions of Eq. (72) quite closely. The velocity increases towards the ice surface, but with a slowing rate due to the stress-dependent flow rate.
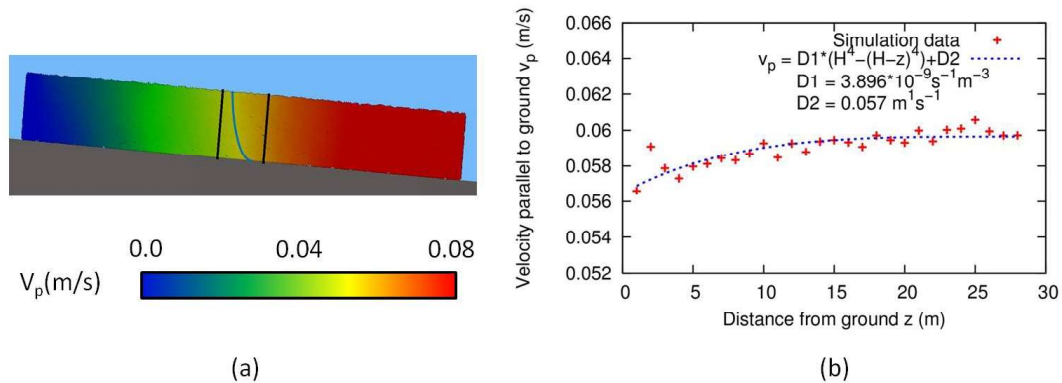

FIGURE 27   (a) The simulation setup for an ice sheet flowing down an inclined surface. The blue curve represents a contour of constant velocity. In (b) the corresponding velocity profile from the middle part of the ice block averaged over the area marked with black lines in (a) is shown. The dotted line is a fit done by using Eq. (72) (Edited from paper II Fig. 10)

As a proof of the model versatility, an ice fall scenario was considered where all the model properties are relevant, namely viscous flow, fracture and fragmentation at the glacier front. An ice fall is a part of a glacier which rapidly moves down a slope partly flowing and partly fracturing. A typical signature of an icefall is a chaotic crevassed surface.
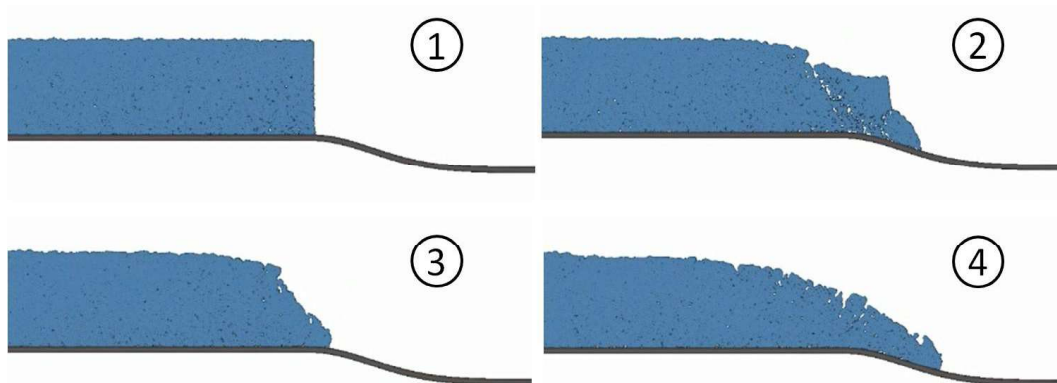

FIGURE 28   Time series of an icefall simulation. The numbers refer to the chronological order of images. (Edited from paper II Fig. 11)

To see if the model is able to qualitatively reproduce typical icefall characteristics, a two-dimensional ice block on a steepening slope was simulated. Four instants of time in such a simulation are shown in Fig. 28. In the beginning (step 1 in Fig. 28) the block is placed in top of the slope and gravity is applied to induce flowing and fragmentation. After some period (step 2) of deformation the stresses in the ice grow too large and a piece of ice is fragmented from the glacier front. In step 3 the detached piece has propagated away from the observed region and the flow continues. As seen moving on from step 3 to step 4 the thinner glacier terminus is less prone to form new fragments and the glacier is able to flow further without detachment. Also, the typical icefall feature of strongly crevassed top surface has become visible.

(a)   (b)
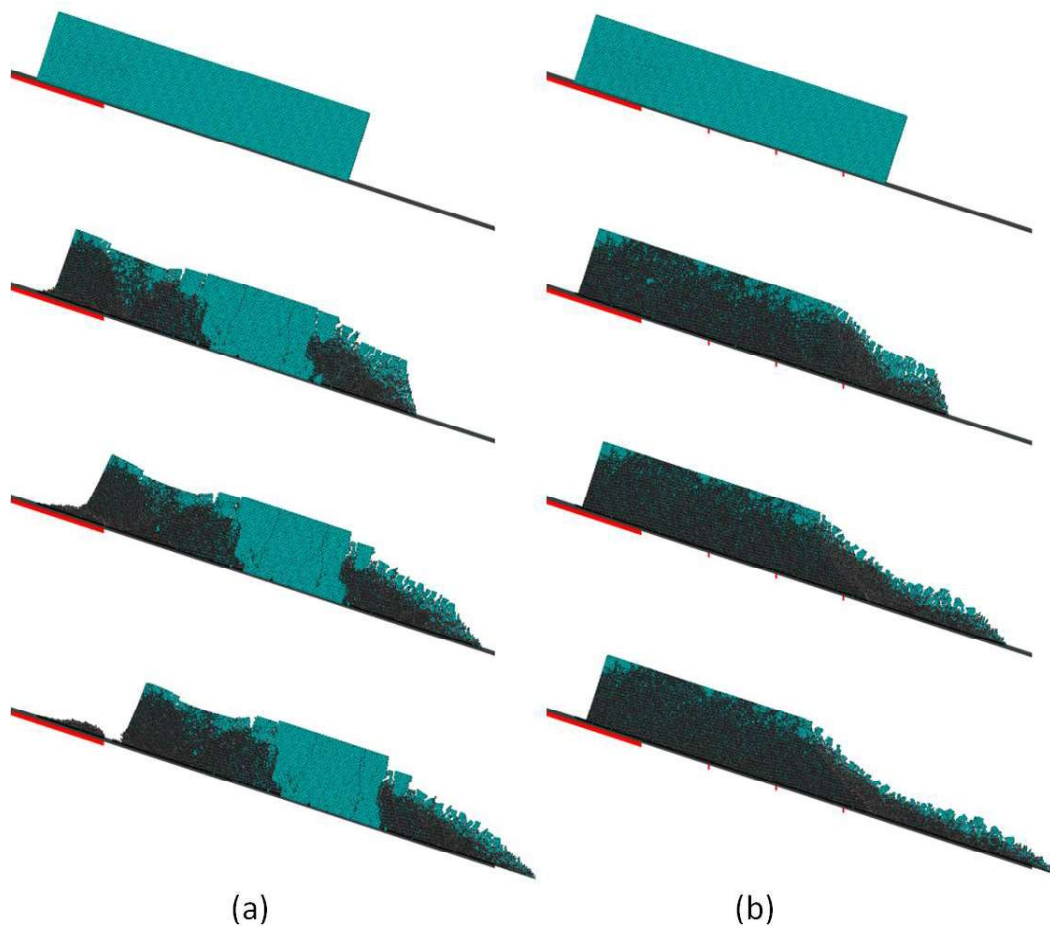
FIGURE 29   Snapshots from surging glacier simulations with frictional contacts (red markers) only in the upper part of the slope (a) and with additional frictional contacts also in the lower part (b). The green colour represent elastic areas where contacting beams are still intact whereas grey areas contain only particles and the beams are broken. (From paper I Fig. 6 and Fig. 7)

The stress dependent breaking and reforming of beams is not the only approach to simulate a viscoelastic material. For some cases it might be sufficient to allow beams to break according to the chosen fracture criterion and the viscous flow

results from the inherent resistance to flow in a granular DEM material. This approach was tested in a simulated surging glacier scenario where a 200 m × 50 m ice block was placed on a 18° slope (Fig. 29). Glacier surges are short-lived events where a glacier advances in a substantially greater velocity than normally (Sevestre 2015).

The viscosity was measured in a separate simulation where all the beams were removed and the material was subjected to a shearing force. With this method a viscosity of 10^5 times lower than in realistic surging glacier was achieved. It is thus expected that the strain rates are an equal factor higher and the time scale can be roughly re-scaled from seconds to days (24 hours = $0.864 \times 10^5 s$). Two different simulations with different bedrock friction configurations were studied. In the first setup (Fig. 29 (a)) the red line in the upper part of the glacier marks a high friction contact whereas in Fig. 29 (b) additional frictional anchors are distributed along the length of the glacier. In addition, a pressure corresponding to the over-burden pressure was applied to the left face of the glacier to simulate the pressure induced by a slab of ice of the same thickness upstream. In Fig. 29 (a) the high friction contact in the upper part is not sufficient to keep the glacier in place and it breaks near the substrate and flows downhill. If the time is re-scaled according to the above explanation the velocity in this scenario reaches roughly 5 m/day which is close to the typical values observed for surging glaciers (Cuffey and Paterson 2010).
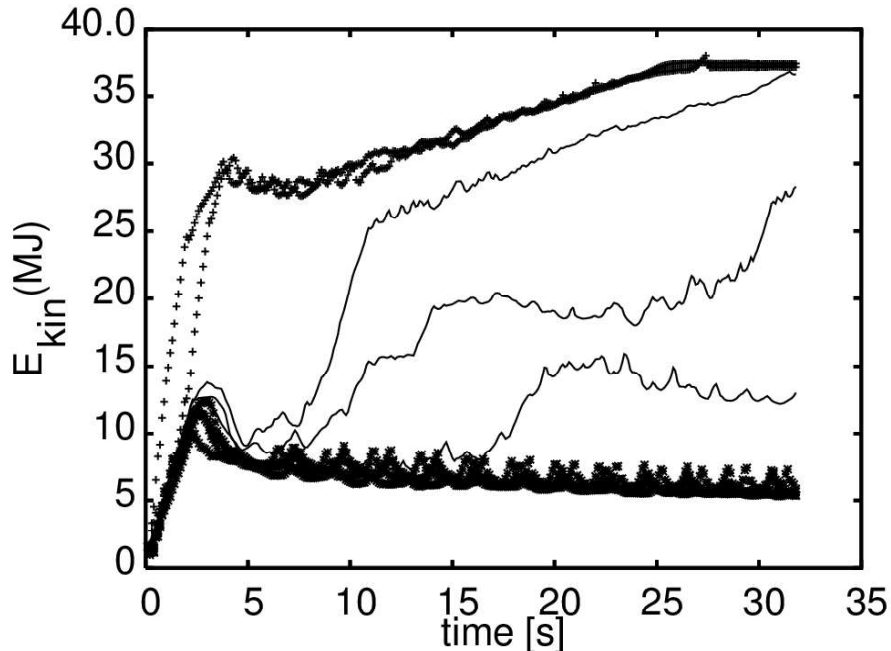

FIGURE 30   Kinetic energy as a function of time for different initial conditions for multiple simulations of setup shown in Fig. 29. The cases with constant surging or quiescent behaviour, discrete markers are used. For the cases of phase transition, continuous lines are used. (From paper I Fig. 8)

In the other case (Fig. 29 (b)), where additional frictional anchors are used, the glacier cannot slide downhill. Instead, only a small part of it near the terminus fractures, fragments and flows a limited distance. As the fragmented layer flows, it gets thinner and the driving force decreases slowing down the flow.

To quantify the above behaviour, kinetic energy (E_{kin}) for multiple simulation runs with varying frictional contact in the slope were recorded. The results are shown in Fig. 30. Two different phases can be recognized according to the kinetic energy of the system. In the low kinetic energy region the system is in a quiescent phase where only a small part of the system fractures and flows downhill (Fig. 29 (b)). In the opposite limit, the entire glacier surges (Fig. 29 (a)) and the resultant kinetic energy reaches much larger values. There exist cases where a process similar to phase transition emerges, when the system starts as a quiescent glacier but during the simulation suddenly starts to surge with a corresponding increase in kinetic energy. Cases where a part of the glacier surges can also be recognized. In these cases, the kinetic energy reaches a value between those typical to quiescent and surging phases.

As seen from the previous approach to surging glaciers, the intrinsic viscosity of granular DEM material can be used in some instances to study viscous behaviour of a material. However, the behaviour is quite uncontrollable as compared to the melting/refreezing kind of viscosity. The granular viscosity exists only when all the beams are broken and elasticity is totally vanished. Thus, a certain single value for viscosity is achieved. In the more elegant melting/refreezing approach presented in section 3.2.3, the viscosity can be controlled much more precisely.

5 CONCLUSIONS

5.1 Summary

In conclusion, a new kind of simulation model was constructed to study the mechanical behaviour of glacier ice. Moreover, the simulation parameters can be freely adjusted to yield a wide variety of material behaviour. The beam stiffness parameters can be controlled to yield elastic properties from soft rubber all the way to the hardest metals. The threshold parameters for individual beams on the other hand can be used to control the material brittleness ranging from sand-like materials to unbreakable substances. In addition, the viscous nature of the material can be controlled via the probabilities for beam breaking and reforming. Even though the modelling of the viscous behaviour was motivated by the Glen's flow law, the probability functions can be easily adjusted to yield a different kind of stress dependence if such is needed. After adjustment of the simulation parameters for glacier ice, the model was used to study multiple glacier ice applications.

The calving behaviour of marine terminating ice fronts, and more specifically the fragment size distribution produced in it, was studied extensively. It was observed that the distributions follow the typical power-law behaviour predicted by crack branching-merging theory of fragmenting materials. It was also observed in some cases that the power-law exponents deviate from the theoretical values of pure crack branching-merging behaviour in the late moments of the calving event indicating the presence of grinding processes. Motivated by this behaviour, a separate more general study beyond the subject of this thesis was conducted to study the grinding behaviour between two shearing surfaces (paper IV).

The waiting time and event size distributions in the calving events were also studied, using simulation results and data acquired from actual glaciers. It was observed that the distributions exhibit power-law behaviour and the power-law exponents are consistent with the exponents of Abelian sandpile models thus indicating that glacier termini can be considered as self-organized critical systems. In this context, a three-dimensional version of the glacier DEM code was also

used but without the viscous behaviour. The focus here was the calving pro-
cesses which are separated by many orders of magnitude in time compared to
viscous flow. Thus omitting the viscous behaviour was well justified.

Several simulations were also conducted to partly validate the viscous flow
behaviour of the model and partly to better understand flow of glacier ice. It was
seen that the model can reproduce the results given by the analytical shallow-
ice equation, that the model material in an icefall scenario strongly resembles the
observed behaviour and that surging glacier behaviour is highly dependent on
the frictional properties of the bedrock-ice interface.

5.2   Outlook

The results obtained in the preceding sections imply that the glacier DEM model
is capable of reproducing a large variety of different glacier ice behaviour. Nev-
ertheless, the model in its current state leaves room for further development. The
most obvious deficiency is the restriction of the full elastic-brittle-viscous model
to two dimensions. There are no fundamental barriers however to make the full
version work in three dimensions.

The problem that cannot be fully corrected at this point is the conflict be-
tween small DEM time step and a long time span of glacier flow. To keep the
simulations stable, a very small time step has to be used and no modern com-
puter can calculate the necessary time span of years in a reasonable time. As was
stated previously, however, the brittle and viscous regimes can be kept well apart
even though they are brought closer together than in real life glaciers. It is also
possible to couple the simulation model with an appropriate FEM model. In this
approach the long periods of ice flow could be simulated with the FEM model
and when the criteria of fracture are met, the system could be switched to DEM
model and vice versa. Some tests to achieve this have already been made but for
a fully working and automatic simulation model more work is needed.

Another problem is related to the grain size of the simulated material. In
the viscous regime of ice deformation, real ice can flow with relatively little resis-
tance because ice can be considered almost continuous in the size scale of glaciers
(the grain size or crystal size is in the sub-millimetre or millimetre scale). For
any sensible simulation however, the grain size has to be in the range of meters.
This induces typical granular effects such as jamming, which was seen in the
early stages of benchmark simulations when compared to Elmer/Ice FEM model.
To overcome this problem, the limit of very small particles can be pursued. Of
course, with the ongoing development of computer efficiency, this becomes more
achievable every day. Alternatively, different approaches where the granularity
does not create problems for viscous flow, could be developed. For example,
in the field of mining sciences a smooth joint model has been used to simulate
the joint between two shearing rock surfaces (Lambert and Coll 2014). In this
approach the intrinsic roughness between two spherical grains is eliminated by

allowing the particles to slide past each other without over-riding one another. All in all, the glacier DEM model provides an alternative to more traditional continuum models in glacier modelling. It has strengths and weaknesses but appears a viable option for describing the behaviour of brittle ice.

REFERENCES

Andrews, R. M. 1985. Measurement of the fracture toughness of glacier ice. Journal of Glaciology 31 (108), 171-176.

Bahr, D. B. 1996. Analytical modeling of glacier dynamics. Mathematical Geology 28 (2), 229-251.

Balevičius, R., Kačianauskas, R., Mroz, Z. & Sielamowicz, I. 2006. Discrete element method applied to multiobjective optimization of discharge flow parameters in hoppers. Structural and Multidisciplinary Optimization 31 (3), 163-175.

Behera, B., Kun, F., McNamara, S. & Herrmann, H. J. 2005. Fragmentation of a circular disc by impact on a frictionless plate. Journal of Physics: Condensed Matter 17, 2439.

Benn, D. I., Hulton, N. R. J. & Mottram, R. H. 2007a. "Calving laws", "sliding laws" and the stability of tidewater glaciers. Annals of Glaciology 46 (1), 123-130.

Benn, D. I., Warren, C. R. & Mottram, R. H. 2007b. Calving processes and the dynamics of calving glaciers. Earth-Science Reviews 82 (3-4), 143-179.

de Berg, M., Cheong, O., van Kreveld, M. & Overmars, M. 2008. Computational Geometry, Algorithms and Applications. Springer-Verlag.

Bidgoli, M. N., Zhao, Z. & Jing, L. 2013. Numerical evaluation of strength and deformability of fractured rocks. Journal of Rock Mechanics and Geotechnical Engineering 5 (6), 419-430.

Borstad, C. P., Khazendar, A., Larour, E., Morlighem, M., Rignot, E., Schodlok, M. P. & Seroussi, H. 2012. A damage mechanics assessment of the Larsen B ice shelf prior to collapse: Toward a physically-based calving law. Geophysical Research Letters 39 (18), 1-5.

Brilliantov, N. V., Spahn, F., Hertzsch, J. M. & Pöschel, T. 1996. A model for collisions in granular gases. Physical Review E 53 (5), 5382-5392.

Burgess, D. O., Sharp, M. J., Mair, D. W. F., Dowdeswell, J. A. & Benham, T. J. 2005. Flow dynamics and iceberg calving rates of Devon Ice Cap, Nunavut, Canada. Journal of Glaciology 51 (173), 219-230.

Carmona, H. A., Wittel, F. K., Kun, F. & Herrmann, H. J. 2008. Fragmentation processes in impact of spheres. Physical Review E 77 (5), 1-10.

Carmona, H. A., Wittel, F. K. & Kun, F. 2014. From fracture to fragmentation with discrete element modeling. The European Physical Journal Special Topics 223, 2369-2381.

66

Chaplin, M. 2016. Ice phases. Water Structure and Science, retrieved in June 2016.

Cuffey, K. M. & Paterson, W. S. B. 2010. The Physics of Glaciers, 4th Edition. Elsevier, Massachusetts, USA.

Cundall, P. A. & Strack, O. D. L. 1979. A discrete numerical model for granular assemblies. Géotechnique 29 (1), 47-65.

Cundall, P. A. 1971. A computer model for simulating progressive, large-scale movements in blocky rock systems. Proceedings of the Symposium of the International Society for Rock Mechanics 2 (8).

Cundall, P. A. 1974. A computer model for rock-mass behavior using interactive graphics for the input and output of geometrical data. National Technical Information Service-report number AD/A-001 602.

Cundall, P. A. 1978. BALL - A program to model granular media using the distinc element method. Technical Note, Advanced Technology Group, Dames & Moore, London.

Depoorter, M. A., Bamber, J. L., Griggs, J. A., Lenaerts, J. T. M., Ligtenberg, S. R. M., van den Broeke, M. R. & Moholdt, G. 2013. Calving fluxes and basal melt rates of Antarctic ice shelves. Nature 502 (7469), 89-92.

Dhar, D. 1999. The Abelian sandpile and related models. Physica A 263 (1-4), 4-25.

Dhar, D. 2006. Theoretical studies of self-organized criticality. Physica A 369 (1), 29-70.

Di Renzo, A. & Di Maio, F. P. 2004. Comparison of contact-force models for the simulation of collisions in DEM-based granular flow codes. Chemical Engineering Science 59 (3), 525-541.

Elliot, S. R. 2000. The physics and chemistry of solids. John Wiley & Sons, Chichester, England.

Fraige, F. Y. & Langston, P. A. 2004. Integration schemes and damping algorithms in distinct element models. Advanced Powder Technology 15 (2), 227-245.

Freireich, B., Kumar, R., Ketterhagen, W., Su, K., Wassgren, C. & Zeitler, J. A. 2015. Comparisons of intra-tablet coating variability using DEM simulations, asymptotic limit models, and experiments. Chemical Engineering Science 131, 197-212.

Gagliardini, O., Zwinger, T., Gillet-Chaulet, F., Durand, G., Favier, L., de Fleurian, B., Greve, R., Malinen, M., Martin, C., Råback, P. J., Ruokolainen, J., Sacchettini, M., Seddik, M. S. H. & Thies, J. 2013. Capabilities and performance of elmer/ice, a new-generation ice sheet model. Geoscientific Model Development 6 (4), 1299-1318.

Gagliardini, O. & Zwinger, T. 2008. The ISMIP-HOM benchmark experiments performed using the Finite-Element code Elmer. The Cryosphere 2, 67-76.

Gammon, P. H., Kiefte, H. & Clouter, M. J. 1983. Elastic constants of ice samples by Brillouin spectroscopy. Journal of physical chemistry 87 (21), 4025-4029.

Gao, R., Du, X., Zeng, Y., Li, Y. & Yan, J. 2012. A new method to simulate irregular particles by discrete element method. Journal of Rock Mechanics and Geotechnical Engineering 4 (3), 276-281.

Ghugal, Y. M. & Sharma, R. 2011. A refined shear deformation theory for flexure of thick beams. Latin American Journal of Solids and Structures 8 (2), 183-195.

Gilbert, A., Gagliardini, O., Vincent, C. & Wagnon, P. 2014. A 3-D thermal regime model suitable for cold accumulation zones of polythermal mountain glaciers. Journal of Geophysical Research: Earth Surface 119 (9), 1876-1893.

Glen, J. W. 1955. The creep of polycrystalline ice. Proceedings of the Royal Society London A 228 (1175), 519-538.

Greve, R. & Heinz, B. 2009. Dynamics of Ice Sheets and Glaciers. Springer, Berlin, Germany.

Hertzberg, R. 1996. Deformation and Fracture Mechanics of Engineering Materials, 4th Edition. John Wiley and Sons, New York, USA.

Inoue, A., Zhang, W., Zhang, T. & Kurosaka, K. 2001. High strength Cu-based bulk glassy alloys in Cu-Zr-Ti and Cu-Hf-Ti ternary systems. Acta Materialia 49 (14), 2645-2652.

Jarosch, A. H. 2008. Icetools: A full Stokes finite element model for glaciers. Computers & Geosciences 34 (8), 1005-1014.

Johnson, J. B., Kulchitsky, A. V., Duvoy, P., Iagnemma, K., Senatore, C., Arvidson, R. E. & Moore, J. 2015. Discrete element method simulations of Mars exploration rover wheel performance. Journal of Terramechanics 62, 31-40.

Johnson, K. L. 1985. Contact mechanics. University Press, Cambridge, England.

Jouvet, G., Picasso, M., Rappaz, J., Huss, M. & Funk, M. 2011. Modelling and numerical simulation of the dynamics of glaciers including local damage effects. Mathematical Modelling of Natural Phenomena 6 (5), 263-280.

Kazerani, T., Zhao, J. & Yang, Z. Y. 2010. Investigation of failure mode and shear strength of rock joints using discrete element method, Rock Mechanics in Cicil and Environmental Engineering - Zhao, Labiouse, Dubt & Mathier (eds). Taylor & Francis Group, London, England.

Kazerani, T. 2013. A discontinuum-based model to simulate compressive and tensile failure in sedimentary rock. Journal of Rock Mechanics and Geotechnical Engineering 5 (5), 378-388.

Kekäläinen, P., Åström, J. A. & Timonen, J. 2007. Solution for the fragment-size distribution in crack-branching model of fragmentation. Physical review E 76 (2), 1-7.

Kruggel-Emden, H., Stepanek, F. & Munjiza, A. 2011. Performance of integration schemes in discrete element simulations of particle systems involving consecutive contacts. Computers & Chemical Engineering 35 (10), 2152-2157.

Kruggel-Emden, H., Sturm, M., Wirtz, S. & Scherer, V. 2008. Selection of an appropriate time integration scheme for the discrete element method (DEM). Computers & Chemical Engineering 32 (10), 2263-2279.

Kun, F. & Herrmann, H. J. 1996. Fragmentation of colliding discs. International Journal of Modern Physics C 7 (6), 837-855.

Kun, F. & Herrmann, H. J. 1999. Transition from damage to fragmentation in collisions of solids. Physical Review E 59 (3), 2623-2632.

Kun, F., Varga, I., Lennartz-Sassinek, S. & Main, I. G. 2013. Approach to failure in porous granular materials under compression. Physical Review E 88 (6), 1-11.

Kun, F., Varga, I., Lennartz-Sassinek, S. & Main, I. G. 2014. Rupture cascades in a discrete element model of a porous sedimentary rock. Physical Review Letters 112 (6), 1-5.

Kwapinska, M., Saage, G. & Tsotsas, E. 2006. Mixing of particles in rotary drums: A comparison of discrete element simulations with experimental results and penetration models for thermal processes. Powder Technology 161 (1), 69-78.

Lambert, C. & Coll, C. 2014. Discrete element modeling of rock joints with a smooth-joint contact model. Journal of Rock Mechanics and Geotechnical Engineering 6 (1), 1-12.

Landau, L. D. 1970. Theory of elasticity. Pergamon Press, Oxford, England.

Lee, J. 1994. Density waves in the flows of granular media. Physical Review E 49 (1), 281-298.

Lee, M. L., Li, Y. & Schuh, C. A. 2004. Effect of a controlled volume fraction of dendritic phases on tensile and compressive ductility in La-based metallic glass matrix composites. Acta Materialia 52 (14), 4121-4131.

Le Meur, E., Gagliardini, O., Zwinger, T. & Ruokolainen, J. 2004. Glacier flow modelling: a comparison of the shallow ice approximation and the full-Stokes solution. Comptes Rendus Physique 5 (7), 709-722.

Liu, C. T., Heatherly, L., Horton, J. A., Easton, D. S., Carmichael, C. A., Wright, J. L., Schneibel, J. H., Yoo, M. H., Chen, C. H. & Inoue, A. 1998. Test environments and mechanical properties of Zr-base bulk amorphous alloys. Metallurgical and Materials Transactions A 29 (7), 1811-1820.

Liu, H. W. & Miller, K. J. 1979. Fracture toughness of fresh-water ice. Journal of Glaciology 22 (86), 135-143.

Lüthi, M. 2013. Physics of glaciers I (course material). Laboratory of Hydraulics, Hydrology and Glaciology, Zürich, Switzerland.

Melheim, J. A. 2005. Cluster integration method in lagrangian particle dynamics. Computer Physics Communications 171 (3), 155-161.

Munjiza, A. 2004. The Combined Finite-Discrete Element Method. John Wiley & Sons, Chichester, England.

Müller, P., Heckel, M., Sack, A. & Pöschel, T. 2013. Complex velocity dependence of the coefficient of restitution of a bouncing ball. Physical Review Letters 110 (25), 1-5.

Nick, F. M., van der Veen, C. J., Vieli, A. & Benn, D. I. 2010. A physically based calving model applied to marine outlet glaciers and implications for the glacier dynamics. Journal of Glaciology 56 (199), 781-794.

Nouguier-Lehon, C., Cambou, B. & Vincens, E. 2003. Influence of particle shape and angularity on the behaviour of granular materials: a numerical analysis. International Journal for Numerical and Analytical Methods in Geomechanics 27 (14), 1207-1226.

O'Sullivan, C. & Bray, J. D. 2004. Selecting a suitable time step for discrete element simulations that use the central difference time integration scheme. Engineering Computations 21 (2-4), 278-303.

Paczuski, M., Boettcher, S. & Baiesi, M. 2005. Interoccurence times in the Bak-Tang-Wiesenfeld sandpile model: A comparison with the observed statistics of solar flares. Physical review letters 95 (18), 1-4.

Peters, B., Džiugys, A., Hunsinger, H. & Krebs, L. 2005. An approach to qualify the intensity of mixing on a forward acting grate. Chemical Engineering Science 60 (6), 1649-1659.

Pöschel, T. & Schwager, T. 2005. Computational granular dynamics. Springer, Heidelberg, Germany.

Pál, G., Varga, I. & Kun, F. 2014. Emergence of energy dependence in the fragmentation of heterogenous materials. Physical Review E 90 (6), 1-8.

Richter-Menge, J. A., Cox, G. F. N. & Perron, N. 1987. The mechanical properties of multi-year sea ice, Phase I: Ice structure analysis. U.S. Army Cold Regions Research and Engineering Laboratory, Hanover, USA.

Rong, G., Liu, G., Hou, D. & Zhou, C. 2013. Effect of particle shape on mechanical behaviors of rocks: A numerical study using clumped particle model. The Scientific World Journal 2013.

70

Rougier, E., Munjiza, A. & John, N. W. M. 2004. Numerical comparison of some explicit time integration schemes usen in DEM, FEM/DEM and molecular dynamics. International Journal for Numberical Methods in Engineering 61 (6), 856-879.

Rubio-Largo, S. M., Janda, A., Zuriguel, I., Maza, D. & Hidalgo, R. C. 2015. Granular flow through an orifice: solving the free fall arch paradox. IV international conference on particle based methods.

Sadd, M. H. 2009. Elasticity—Theory, Applications and Numerics, 2nd edition. Academic Press, Burlington, USA.

Salzmann, C. G., Radaelli, P. G., Hallbrucker, A., Mayer, E. & Finney, J. L. 2006. The preparation and structures of hydrogen ordered phases of ice. Science 311 (5768), 1758-1761.

Sator, N. & Hietala, H. 2010. Damage in impact fragmentation. International Journal of Fracture 163 (1), 101-108.

Sator, N., Mechkov, S. & Sausset, F. 2008. Generic behaviours in impact fragmentation. Europhysics Letters 81 (4), 1-6.

Schulson, E. M. & Duval, P. 2009. Creep and fracture of ice. Cambridge University Press, Cambridge, England.

Seon, M. H., Benaroua, H. & Wei, T. 1999. Dynamics of transversely vibrating beams using four engineering theories. Journal of Sound and Vibration 225 (5), 935-988.

Sevestre, H. 2015. Surge-type glaciers: controls, processes and distribution. PhD thesis, University of Oslo, Norway.

Shi, G. H. 1992. Discontinuous deformation analysis: A new numerical model for the statics and dynamics of deformable block structures. Engineering Computations 9 (2), 157-168.

Shäfer, J., Dippel, S. & Wolf, D. E. 1996. Force schemes in simulations of granular materials. Journal de Physique I 6 (1), 5-20.

Smeets, B., Odenthal, T., Vanmaercke, S. & Ramon, H. 2015. Polygon-based contact description for modeling arbitrary polyhedra in the discrete element method. Computer Methods in Applied Mechanics and Engineering 290, 277-289.

Sochor, M. 1998. Strength of materials I. CTU Publishing House, Prague, Czech Republic.

Sundaram, S. & Collins, L. R. 1996. Numerical considerations in simulating a turbulent suspension of finite-volume particles. Journal of Computational Physics 124 (2), 337-350.

Taguchi, Y.-h. 1992a. New origin of a convective motion: Elastically induced convection in granular materials. Physical Review letters 69 (9), 1367-1370.

Taguchi, Y.-h. 1992b. Powder turbulence: direct onset of turbulent-flow. Journal de Physique II 2 (12), 2103-2114.

Takeuchi, S., Wang, S. & Rhodes, M. 2004. Discrete element simulation of a flat-bottomed spouted bed in the 3-D cylindrical coordinate system. Chemical Engineering Science 59 (17), 3495-3504.

Thompson, P. A. & Grest, G. S. 1991. Granular flow: Friction and the dilatancy transition. Physical Review Letters 67 (13), 1751-1754.

Thomson, C., Lue, L. & Bannerman, M. N. 2014. Mapping continuous potentials to discrete forms. Journal of Chemical Physics 140 (034105), 1-9.

Thornton, C., Yang, F. & Seville, J. 2015. A DEM investigation of transitional behaviour in gas-fluidised beds. Powder Technology 270 (A), 128-134.

Timár, G., Kun, F., Carmona, H. A. & Herrmann, H. J. 2012. Scaling laws for impact fragmentation of spherical solids. Physical Review E 86 (1), 1-7.

Timco, G. W. & Frederking, R. M. W. 1996. A review of sea ice density. Cold Regions Science and Technology 24 (1), 1-6.

Timco, G. W. & Weeks, W. F. 2010. A review of the engineering properties of sea ice. Cold Regions Science and Technology 60 (2), 107-129.

Timár, G., Blömer, J., Kun, F. & Herrmann, H. J. 2010. New universality class for the fragmentation of plastic materials. Physical Review Letters 104 (9), 1-4.

Tsuji, Y., Tanaka, T. & Ishida, T. 1992. Lagrangian numerical simulation of plug flow of cohesionless particles in a horizontal pipe. Powder Technology 71 (3), 239-250.

Verma, D., Kakkar, N. & Mehan, N. 2014. Comparison of brute-force and k-d tree algorithm. International Journal of Advanced Research in Computer and Communication Engineering 3 (1), 5291-5297.

Vieli, A., Payne, A. J., Du, Z. & Shepherd, A. 2006. Numerical modelling and data assimilation of the Larsen B ice shelf, Antarctic Peninsula. Philosophical Transactions of the Royal Society A 364 (1844), 1815-1839.

Walter, F., O'Neel, S., McNamara, D., Pfeffer, W. T., Bassis, J. N. & Fricker, H. A. 2010. Iceberg calving during transition from grounded to floating ice: Columbia Glacier, Alaska. Geophysical Research Letters 37 (15), 1-5.

Weeks, W. & Assur, A. 1967. The mechanical properties of sea ice. U.S. Army Cold Regions Research & Engineering Laboratory, Monograph II-C3, Hanover, USA.

Williams, J. R., Hocking, G. & Mustoe, G. G. W. 1985. Theoretical basis of the discrete element method. NUMETA 1985, Numerical Methods ofEngineering, Theory and Applications, A.A. Balkema, Rotterdam, Netherlands.

Wiącek, J. & Molenda, M. 2014. Effect of particle polydispersity on micromechanical properties and energy dissipation in granular mixtures. Particuology 16, 91-99.

Wolff, M. F. H., Salikov, V., Antonyuk, S., Heinrich, S. & Schneider, G. A. 2013. Three-dimensional discrete element modeling of micromechanical bending tests of ceramic-polymer composite materials. Powder Technology 248, 77-83.

Zehnder, A. T. 2012. Fracture mechanics. Springer, London, England.

Zemp, M., Nussbaumer, S. U., Naegeli, K., Gärtner-Roer, I., Paul, F., Hoelzle, M. & Haeberli, W. 2013. Glacier Mass Balance Bulletin No. 12 (2010-2011). Staffel Druck AG, Zurich, Switzerland.

Zhang, L., Quickley, S. F. & Chan, A. H. C. 2013. A fast scalable implementation of the two-dimensional triangular discrete element method on a GPU platform. Advances in Engineering Software 60-61, 70-80.

Zhang, Y. & Campbell, C. S. 1992. The interface between fluid-like and solid-like behaviour in two-dimensional granular flows. Journal of Fluid Mechanics 237, 541-568.

Zhang, Z. F., Eckert, J. & Schultz, L. 2003. Difference in compressive and tensile fracture mechanisms of $Zr_{59}Cu_{20}Al_{10}Ni_8Ti_3$ bulk metallic glass. Acta Materialia 51, 1167-1179.

Zhang, Z. F. & Eckert, J. 2005. Unified tensile fracture criterion. Physical Review Letters 94 (9), 1-4.

Zwinger, T. & Moore, J. C. 2009. Diagnostic and prognostic simulations with a full Stokes model accounting for superimposed ice of Midtre Lovénbreen, Svalbard. The Cryosphere 3, 217-229.

Åström, J., Vallot, D., Schäfer, M., Welty, E., O'Neel, S., Bartholomaus, T., Liu, Y., Riikilä, T., Zwinger, T., Timonen, J. & Moore, J. C. 2014. Termini of calving glaciers as self-organized critical systems: Calving event catalogue. Nature Geoscience 7, 874-878.

Åström, J. 2006. Statistical models of brittle fragmentation. Advances in Physics 55 (3-4), 247-278.

Åström, J. A. & Herrmann, H. J. 1998. Fragmentation of grains in a two-dimensional packing. The European Physical Journal B 5 (3), 551-554.

Åström, J. A., Holian, B. L. & Timonen, J. 2000. Universality in fragmentation. Physical Review letters 84 (14), 3061-3064.